

MODELING OF NANO-SCALE FRACTURE MECHANISMS IN A GRAPHENE SHEET  
USING THE ATOMISTIC J-INTEGRAL

by

ANUBHAV ROY

SAMIT ROY, COMMITTEE CHAIR  
VINU UNNIKRISHNAN  
PAUL G. ALLISON

A THESIS

Submitted in partial fulfillment of the requirements  
for the degree of Master of Science  
in the Department of Aerospace Engineering and Mechanics  
in the Graduate School of  
The University of Alabama

TUSCALOOSA, ALABAMA

2018

Copyright Anubhav Roy 2018  
ALL RIGHTS RESERVED

## ABSTRACT

Researchers have performed studies with the addition and dispersion of a few weight percent of nanoscale particles in polymer matrices to mitigate the brittleness and microcracking of polymer matrices without incurring weight penalty and improve their strain to failure and fracture toughness. This thesis aims at studying these length scale effects in nano-fillers, identifying the existence of a lower bound on flaw-size that marks the transition from brittle fracture to strength-based failure in nanocomposites, resulting in a deviation from linear elastic fracture mechanics (LEFM) predictions. Crack-tip bond-order based prediction of critical value of stress intensity factor is also addressed in this work. The objective of this work also includes employment of an atomistic J-integral as a suitable metric for the evaluation of fracture behaviour in materials at nanoscale. Good agreement is observed between atomistic and LEFM predictions using far-field stress and J-integral computations. While the far-field stress based atomistic data enables global prediction of the system undergoing fracture, the J-integral around the crack tip sheds light on local near-crack-tip stress state. Both far-field and near tip predictions are seen to deviate from LEFM predictions below a certain length-scale. In addition, effects such as nonlocality in molecular dynamics (MD) computations and entropic effects at the atomistic scale add to the discrepancy with LEFM. The fracture study on crystalline (graphene) was performed to lay the foundation for atomistic predictions of fracture in amorphous (polymer) nanocomposite systems.

## **DEDICATION**

This thesis is dedicated to everyone who helped me and guided me through the trials and tribulations of creating this manuscript, particularly, my parents Mr. Joydeep Roy and Mrs. Baishali Roy and my close friends Shivank Shah, Soham Gupta, Soumya Goswami, Sumit Gupta and Bratati Som who stood by me throughout the time taken to complete this thesis.

## LIST OF ABBREVIATIONS AND SYMBOLS

<i>MD</i>	Molecular Dynamics
<i>LEFM</i>	Linear Elastic Fracture Mechanics
<i>ReaxFF</i>	Reactive Force Field
<i>LAMMPS</i>	Large-scale Atomic/Molecular Massively Parallel Simulator
<i>J<sub>IC</sub></i>	Critical Value of J-integral for a Mode-I fracture
<i>K</i>	Stress Intensity Factor
<i>k</i>	Bond Energy Constant
<i>BO</i>	Bond Order

## **ACKNOWLEDGMENTS**

I would first like to express deep gratitude to my advisor, Dr. Samit Roy, for his constant guidance and support through-out the research for this thesis. His insights and technical guidance were of great help during the entire research. I would like to thank Dr. Vinu Unnikrishnan for helping and guiding me with the molecular dynamics simulations. His knowledge and help were extremely useful in successfully completing the simulations. I would also like to thank Dr. Paul G. Allison for serving on my thesis committee. I would like to acknowledge sponsorship of this research by the AFOSR Low Density Materials Program, Contract No. FA9550-18-1-0084. I would like to thank my groupmates and colleagues Mr. Pruthul Ravindranath, Mr. Bodiuzzaman Jony, Mr. Rakesh Mothukuru, Mr. Zaheer Muhammed, and Mr. Nilesh Vishe for always lending a helping hand and their motivation throughout this research. I would also like to thank all my friends for their constant support and encouragement. Finally, I express my deep acknowledgments and respect to my parents, Mr. Joydeep Roy and Mrs. Baishali Roy who have always blessed me and have been a source of moral support, inspiration and encouragement.

## CONTENTS

ABSTRACT .....	ii
DEDICATION .....	iii
LIST OF ABBREVIATIONS AND SYMBOLS .....	iv
ACKNOWLEDGMENTS .....	v
LIST OF TABLES .....	x
LIST OF FIGURES .....	xi
CHAPTER 1 INTRODUCTION .....	1
1.1 Background .....	1
1.2 Objectives .....	5
1.3 Outline .....	7
CHAPTER 2 LITERATURE REVIEW .....	9
2.1 Nanoscale modelling of fracture in graphene .....	10
2.2 Nonlocal Effects at the Atomistic Scale .....	10
2.3 Atomistic J-integral .....	11
CHAPTER 3 MOLECULAR DYNAMICS SIMULATIONS .....	14
3.1 Introduction .....	14
3.2 Molecular Dynamics Simulation Procedure .....	15
3.3 Numerical Integration Algorithms .....	16
3.3.1 Verlet Algorithms .....	16
3.3.2 Leap-frog Algorithms .....	17

3.3.3	Beeman’s Algorithms.....	18
3.3.4	Velocity-Verlet Algorithms .....	18
3.4	Thermostats.....	19
3.4.1	Anderson Thermostats .....	20
3.4.2	Berendsen Thermostats.....	20
3.4.3	Nose-Hoover Thermostats .....	20
3.5	Barostats.....	21
3.6	Ensembles .....	21
3.6.1	NVE ensemble .....	21
3.6.2	NVT ensemble .....	22
3.6.3	NPT ensemble.....	22
3.7	Boundary Conditions .....	22
3.8	Potential Functions.....	23
3.8.1	Reactive Force Field (ReaxFF) .....	25
3.9	Overview of LAMMPS.....	27
3.10	OVITO .....	28
CHAPTER 4 THEORETICAL BACKGROUND.....		29
4.1	Flaw Size Insensitivity.....	29
4.2	Effect of non-locality in nanoscale .....	30
4.3	Quantized Fracture Mechanics .....	31
4.4	Different modes of fracture and their continuum quantification .....	32
4.5	J-integral and its atomistic evaluation methodology .....	33
4.5.1	Evaluation of energy density field (U).....	36

4.5.2	Evaluation of Displacement gradient.....	37
4.5.3	Evaluation of First Piola-Kirchhoff Stress.....	37
4.6	Atomistic J-integral at Finite Temperature.....	39
4.6.1	Evaluation of Dynamical Matrix .....	41
4.7	Numerical Evaluation of Atomistic J-integral .....	44
CHAPTER 5 MODELLING AND SIMULATION.....		48
5.1	Modelling module.....	48
5.2	Energy-minimization module .....	48
5.3	Thermal equilibration module.....	49
5.4	Modelling discrete crack for defected sheets.....	49
5.5	Isothermal uniaxial tensile straining module .....	50
5.6	Post-processing module .....	52
CHAPTER 6 RESULTS AND DISCUSSIONS.....		53
6.1	Isothermal Straining.....	53
6.2	Length-scale effect of flaw size in nanoscale .....	56
6.3	Comparison with QFM predictions .....	57
6.4	Non-local effect in nanoscale.....	58
6.5	Atomistic J-integral with and without the effect of entropy .....	59
6.5.1	Choice of box size.....	60
6.5.2	Choice of radius of influence cloud.....	61
6.5.3	Validation of path independence of J-integral .....	61
6.5.4	Computation of $J_2$ component.....	63
6.5.5	Path Independence of the entropic component .....	63

6.5.6	Computed $J_I$ vs $K_I$ with and without considering entropic effects.....	64
6.5.7	Tracking Internal Energy Density (U), First Piola Kirchoff Stress (P) and Displacement Gradient Tensor at crack initiation and during crack growth .....	66
CHAPTER 7 CONCLUSION AND FUTURE WORK .....		69
REFERENCES .....		72

## LIST OF TABLES

TABLE 4.1 : Sample values of J-integral computed for graphene at 300 K.....	47
TABLE 6.1 : Relationship between lattice removal and crack length.....	53

## LIST OF FIGURES

Figure 1.1: Compact tension fracture test results for baseline and nanographene reinforced EPON 862 epoxy specimens (at room temperature).....	2
Figure 1.2: Improvement of normalized mixed mode fracture envelop for epoxy Nano-composite with increased reinforcement .....	2
Figure 3.1: Flowchart of a MD process .....	15
Figure 3.2: Ensembles.....	21
Figure 3.3: Schematic illustrating a 3D simulation box with Periodic Boundary Conditions in all directions .....	23
Figure 3.4: Schematic plot between Bond Order and Interatomic Distance.....	26
Figure 4.1: Crack length effect at the nanoscale leading to a brittle to ductile transition .....	29
Figure 4.2: Nonlocal effect at nanoscale.....	31
Figure 4.3: Three modes of fracture .....	32
Figure 4.4: Illustration of a localization box with atom $\alpha$ inside and atom $\beta$ outside the box.....	34
Figure 4.5: Evaluation of ReaxFF equivalent energy constant K.....	44
Figure 4.6: Gaussian quadrature points along the integration contour depicting localization boxes on one side .....	45
Figure 4.7: 9-noded Finite Element framework for computation at the Gauss Points .....	46
Figure 5.1: Modelled graphene sheet in VMD .....	48
Figure 5.2: A 30.59 Å crack is created at the center of the sheet removing 11 hexagonal lattices.....	50
Figure 5.3: A typical center-cracked sheet undergoing isothermal tensile straining.....	51
Figure 6.1: a) n=0 initial state; b) n=11 initial state; c) n=0 after failure; d) n=11 after failure. ....	54
Figure 6.2: (a) Far-field stress (blue line) as a function of applied strain for n=5. (b) Far-field stress (blue line) as a function of applied strain for n=11. Failure occurs when bond-order goes to zero as shown by the green line .....	55

Figure 6.3: Stress at failure for each case of initial half-crack lengths.....	56
Figure 6.4: Accuracy of atomistic predictions in computing quantized far-field stresses. ....	58
Figure 6.5: Existence of finite valued stress at crack tip. ....	58
Figure 6.6: Evolution of finite traction at the crack face. ....	59
Figure 6.7: Influence of localization box size on computed stress values for graphene.....	60
Figure 6.8: Effect of radius of influence cloud on computed stress values for graphene.....	61
Figure 6.9: Concentric contours for validation of Path-Independence. ....	62
Figure 6.10: Path Independence of atomistic $J_U$ (Energetic Component). ....	62
Figure 6.11: Non-existence of the path independent y-y component of atomistic $J_U$ .....	63
Figure 6.12: Path Independence of atomistic $J_\eta$ (Entropic Component).....	64
Figure 6.13: Atomistic J-integral computations in graphene with zig-zag morphology as a function of $K_I$ for purely energetic contribution and total (with energetic and entropic) contributions at 300K shown along with change in Bond Order at the crack tip. ....	66
Figure 6.14: Computed (a) internal energy density (U), components of (b) displacement gradient tensor ( $H_{11}$ ), (c) first Piola-Kirchoff stress tensor ( $P_{11}$ ) with incremental strain shown along with varying Bond Order at crack tip for center crack length of 30.95 Å.....	68
Figure 7: Schematic of a hierarchical multiscale model for analysis of structures .....	71

# CHAPTER 1

## INTRODUCTION

### 1.1 Background

Composites have numerous advantages over conventional material systems in terms of higher specific stiffness and specific strength, reduced easier installation costs coupled with lower life-cycle costs and improved safety. All these advantages have contributed to the global acceptance of composite materials in diverse applications in the fields of aerospace, automotive, and infrastructure. Due to considerable reduction of structural weight leading to significant fuel savings, composites have been finding its extensive use in aerospace industry. The Boeing 787 contains almost 50% composites of its total weight in carbon composites. The reason why CFRP is often used for primary airframe structures is because of its high specific stiffness and strength ratio, tailor ability, light- weight, good corrosion resistance and radar absorption, and ease of manufacturing.

This clearly indicates a trend of increasing use of various types of composites, accompanied by a decreasing use of metals in aerospace structures. Advanced composites are also being used in high performance automobile components, as well as infrastructural applications. Reduced emission due to enhancement in fuel efficiency is achieved by considerable reduction of weight of the car without compromising performance.

Recent years have witnessed notable improvement in mechanical properties of nano-reinforced polymer composites [1-5]. Compact-tension (CT) fracture tests conducted by Kumar

et. al [6] corroborate these observations, as presented in Figure 1.1, showing an increase in peak failure load by 141% and 190% and a corresponding increase in fracture toughness by 142% and 200% over baseline specimens at room temperature for EPON-862 epoxy modified with mere 0.1 wt.% and 0.5 wt.% nano-graphene respectively.

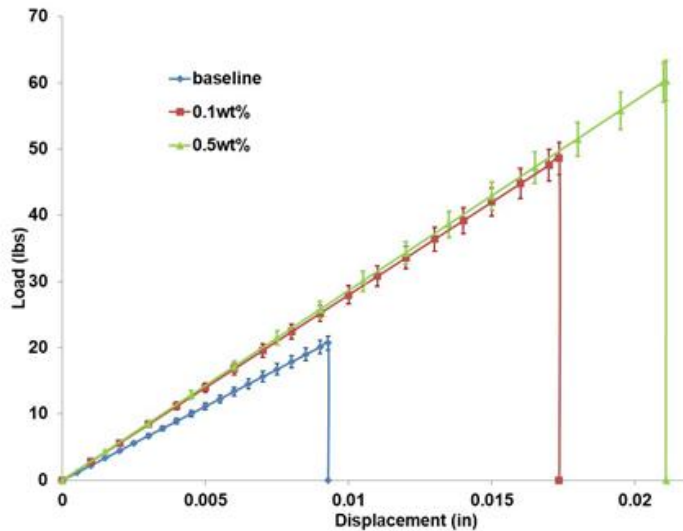


**Figure 1.1:** Compact tension fracture test results for baseline and nanographene reinforced EPON 862 epoxy specimens (at room temperature) [6]

Quasi-static fracture studies

published in work of Kumar et al. [7] has shown remarkable improvement in each mode mix case as depicted in the mixed-mode fracture toughness envelop shown in Figure 1.2.

Other researchers [8] have also reported similar observations of

improvement in fracture properties of graphene reinforced epoxy and the enhancement was attributed to deflection of the crack due to the presence of graphene. The observed improvement of

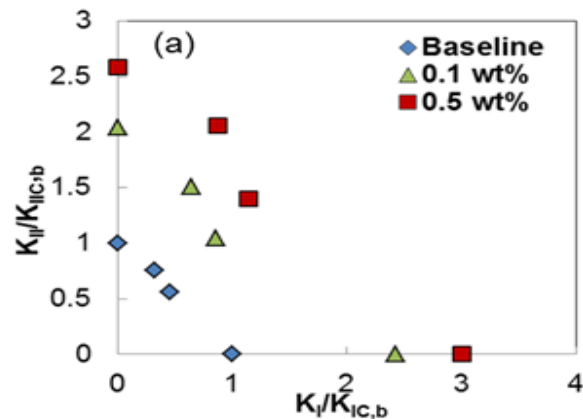


**Figure 1.2:** Improvement of normalized mixed mode fracture envelop for epoxy nano-composite with increased reinforcement [7]

properties at macroscale appears to be due to nanoscale interactions between the constituent materials, which cannot be explained by a simple micro-mechanics model based on the rule-of-mixtures. Consequently, the fundamental mechanism(s) responsible for this enhanced fracture toughness at the nanoscale is still not well understood.

Nanoscale simulations are required to be performed to understand this local influence of nanoparticles on the nanocomposite system. But modeling a macro-system with purely nanoscale modeling quickly becomes computationally intractable. Hence, multi-scale models need to be developed to bridge this disparity in length and time scales. Appropriate computational tools such as molecular dynamics at nanoscale, generalized method of cells at micro-scale and finite element analysis at macro-scale could be used to effectively transfer information from one length scale to the other to reduce the total computation time.

MD simulations can be viewed as a bridge between the deterministic and local behaviour of the macroscopic material system and the nonlocal statistical nature of atomistic interactions. MD offers us possibility to predict the time evolution of a system of interacting particles and estimate the relevant physical properties. Nowadays, MD (as well as Density Functional Theory (DFT)) is frequently used in analysing atomistic-scale behaviour of materials since it is able to capture complex interactions of particles at molecular level and help us to better understand the Nano-scale phenomena including energetic and entropic effects at elevated temperature.

In conventional macro-scale continuum fracture mechanics, the J-integral is defined as the divergence of the Eshelby energy-momentum tensor and has been widely used to quantify the crack driving force available from thermo-mechanical loading as well as material inhomogeneities. One advantage of using J-integral over other fracture metrics such as strain energy release rate (G) is that the J-integral is applicable even in the presence of significant

material nonlinearity. However, in order to extend the concept of the continuum J-integral to the atomistic domain, the following key issues must be resolved: (a) computation of continuous variables, such as displacement and their derivatives, from discrete atomistic quantities, (b) including nonlocality in J that is inherent in atomistic computations due to long range inter-atomic forces, and (c) incorporating entropic effects due to thermal motion in a atomistic system which is not present in conventional continuum description. The framework of the atomistic J-integral fully allows for finite deformation thermo-mechanics, nonlocality inherent in MD, and entropic effects due to the thermal motion of atoms at elevated temperature. In 2014, Zhang et. al [9] performed molecular dynamics (MD) simulation on monolayer single-crystal center-cracked graphene sheet with different crack lengths to determine the effect of nano-size crack length on fracture energy. They concluded from their simulations that linear elastic fracture mechanic (LEFM) is valid for graphene because  $\sigma_c \sqrt{a_0} \approx \sqrt{2\gamma E / \pi} = \text{constant}$ , where  $\sigma_c$  is the critical far-field stress at fracture initiation,  $a_0$  is the half crack length,  $\gamma$  is the energy per unit area to form a new surface, and E is the Young's modulus of graphene. However, it is evident from their simulation data that this is true only for total crack lengths greater than ~10 nm. There is significant deviation from LEFM below this crack length due to a gradual transition from brittle fracture to strength based (ductile) failure. Several researchers have recently investigated this nanoscale flaw- size effect [10-13] and have concluded that there exists flaw size insensitivity, and therefore, deviation from LEFM at the nanoscale. Others have found that the flaw size insensitivity at the nanoscale does not exist [14]. Predictions obtained using the atomistic J are compared with LEFM predictions to underscore the flaw size effect for the case of a single (zig-zag) graphene sheet with a center crack under tensile loading at elevated temperature s. Further, the investigation into nanoscale flaws in graphene and CNT led to the development of quantized

fracture mechanics (QFM) which states that the discrete nature of crystal lattice should only allow certain discrete value of critical energy release rate, with forbidden bands in between [10].

This thesis deals with the nanoscale study of a nano-graphene system. A methodology to study fracture at atomistic level is discussed. Fracture toughness of a material is related to the critical value of J-integral, therefore, J-integral will be used as a metric for estimating the crack driving force as well as the fracture toughness of the material in this dissertation. Though fracture can be characterized through parameters such as strain energy release rate (G), stress intensity factor (K) they are applicable only in the linear and elastic range of the stress-strain response of the material. On the other hand, J-integral is identical to G in the linear range but has the advantage of being applicable in the nonlinear range as well as being path independent. Also, the critical value of J-integral is directly related to fracture toughness of the material. Because it is now well-established that the complex interactions at molecular level can only be understood by numerical methods which appeal to theoretical formalisms at the nanoscale, molecular dynamics (MD) will be used to analyze and understand nano-scale fracture phenomena. The ability to simulate a large number of atoms (atomic systems simulated by MD are typically much larger ab-initio methods [14] allows us to have better statistical estimates of system thermodynamic properties such as thermal conductivity and mechanical properties such as the Young's modulus. By retaining the level of detail required to describe the structure of atomic systems coupled with the selection of proper force-field parameters to accurately describe the various molecular interactions [15] the necessary bulk properties of any system can be closely simulated.

## **1.2 Objectives**

Nano-graphene reinforced polymer nanocomposites proved to be one of the toughest

materials under subjections to fracture. Therefore, it needs to be figured out how the nanoparticles can be employed as matrix reinforcement of optimized size to maintain a flaw size less than the critical value such that debond cracks along nanoparticle-polymer interface will remain below a critical length scale thereby enhancing toughness of the nano-composite in macro-scale phase of the multi-scale model. In other words, the percentage of nano-graphene reinforcement needs to be optimized for the system to exhibit maximum toughness against fracture. But molecular dynamics (MD) being the most fundamental phase of the multiscale model, the first and the most essential step of encountering the problem is to analyze the most fundamental particle of the system, which is a nano-graphene in MD environment.

Existence of a finite valued far-field critical-stress, known as theoretical strength, corresponding to failure of a material system even with a zero-length of crack (pristine case), has been recognized in this thesis as opposed to LEFM prediction of stress tending towards infinity for a limiting case of no-crack. Based on this above recognition, the critical half-length of an initial crack, was theoretically evaluated, that needs to be present in a material system, to mark the transition from damage induced failure (based on theoretical strength) to fracture induced failure (based on initial crack length). For a strong nanomaterial like Graphene, the theoretical critical half-length of crack was found to be  $1.33\text{\AA}$ . Essentially being a length-scale effect, this demands a thorough investigation of nano-mechanical behavior of the material system

The objective of this thesis is to investigate the observed deviation of atomistic predictions from LEFM predictions for nano-scale flaw sizes in graphene. It aims at understanding the mechanisms behind the length-scale based crack size effect on far-field critical stress (failure strength) at the nanoscale. The key issues to be investigated in this thesis are: (a) flaw size effect, (b) non-local effects due to the long-range inter-atomic forces which can result in the existence

of finite stresses at crack tip and finite traction on crack faces, (c) entropic effects due to the random thermal motion of atoms. In addition, the thesis will investigate Quantized Fracture Mechanics (QFM) based prediction of post-initiation stresses for discrete openings of lattice for self-similar crack growth cases, bond order based prediction of fracture toughness of the nano-graphene, and development and application of an atomistic J-integral vector incorporating the above attributes (a-c) including entropic effects as a suitable metric for the evaluation of fracture behavior in materials at the nanoscale and their stated deviations from LEFM prediction.

Specifically, the J-integral will be employed in this thesis to investigate flaw-tolerance at the nanoscale reported by many researchers, as well as to develop a methodology to *predict* the initiation fracture toughness of the material and the resistance to fracture as a function of crack length. For this purpose, a bond-order based potential (ReaxFF) available in LAMMPS molecular dynamics (MD) software will be utilized to accurately pinpoint bond separation. Predictions obtained using the atomistic J will be compared with LEFM predictions to underscore the flaw size effect for the case of a single (zig-zag) graphene sheet with a center crack under tensile (Mode-I) loading.

### **1.3 Outline**

The thesis consists of six chapters. Chapter 1 presents background and motivation for the current work. Advantages, applications of composites and the need for multi-scale analysis of composites are discussed in that chapter. A review of literature relevant to the current research is presented in Chapter 2. Chapter 3 provides a discussion of the basic concepts of molecular dynamics simulations. The underlying theories, along with various parameters involved in MD are discussed. A brief discussion of the software, LAMMPS, used for MD simulations is also presented in that chapter.

A detailed discussion of the theoretical background and methodologies are presented in

Chapter 4. This chapter includes the idea of deviation of atomistic predictions from LEFM and equations pertaining to evaluation of theoretical critical flaw-dimension. It also includes the methodologies adopted to implement the QFM predictions to this problem based on bond-order and discusses the approach used for evaluating J-integral at the nanoscale. Formulae for using discrete atomistic data to obtain the parameters involved in J-integral are presented, along with the numerical evaluation methodology. To verify the methodology, J-integral was computed for a nanoscale graphene sheet under Mode-I loading. The detailed procedures of modelling and simulation are presented in Chapter 5. The results of all these studies are presented and discussed in Chapter 6. The chapter is divided into two parts. The effect of localization box size and radius of influence necessary for calculation of atomistic J-integral were investigated and discussed in this chapter. Chapter 7 contains a summary discussion of all the results obtained, original contributions of this work, along with scope for future work.

## **CHAPTER 2**

### **LITERATURE REVIEW**

Recent years have witnessed the versatility of carbon fibers, graphene and nano-graphene reinforced polymer composites for its diverse applications in aerospace, automobile, bio-medical, infrastructure and sports equipment. There is a need for more research on polymers for a better understanding of their mechanical properties and tailor-ability for their application to a particular field. Significant contributions have been made by the scientific community towards not only developing various techniques to enhance mechanical properties, but also the fundamental ways in which they are studied and analyzed, i.e. the shift towards methods of computational modeling.

Experimental studies have indicated that the mechanical properties of polymers can be improved to a significant extent by using nano-fillers and improving the processing of these nano-composites. The computational efficiency has facilitated modeling of these nanocomposites in extreme details, especially at the nanoscale using methods like molecular dynamics, which is important for understanding the mechanisms responsible for property enhancement using nano-fillers. The most fundamental and primary step of this understanding comes from the detailed atomistic study of the mechanical response of the nano-fillers, which in this case are nano-graphene platelets. A lot of research has been conducted in recent years to study the mechanical properties as well as drawing atomistic observations of graphene as a material. A comprehensive

review of previous work in these areas is presented in this chapter.

## **2.1 Nanoscale modelling of fracture in graphene**

Modelling particle interactions at the nanoscale requires approaches that can account for the complex, nonlinear constitutive behaviour at this length scale. Molecular Dynamics (MD) has been proven effective in capturing the typical phenomena related to fracture at the nanoscale [16-22]. Abraham et al. [23] successfully demonstrated the ability of molecular dynamics (MD) for simulating fracture in large scale atomic systems. Atomic systems containing million atoms (in 2D lattice) were used to simulate brittle and ductile materials using Lennard-Jones and embedded-atom potentials respectively. A comparison between experimental and computational observations was made. Computationally observed phenomena like dynamic instability of crack tip and were found to comply with laboratory findings. In another article by Abraham [24] a detailed discussion of simulating crack propagation in solids using molecular dynamics is presented. The discussion focusses on crack dynamics and the propagation speed of crack. It was noted that a brittle crack starts propagating in a straight line, but the motion becomes erratic due to instabilities in the dynamics of the crack. Also, this transition occurs at one-third of the Rayleigh wave speed. This behavior was found to be independent of the material properties, imperfections and interatomic potentials. MD was also used to study the properties of graphene and to understand fracture behavior at nanoscale [15]. Thermodynamic and mechanical properties can be estimated via statistical mechanics using MD if a sufficient number of atoms are included in the molecular model and the simulation is carried out for a long enough time span, in accordance with the ergodic principle [25].

## **2.2 Nonlocal Effects at the Atomistic Scale**

Significant deviations from continuum based LEFM predictions can occur in the

atomistic domain due to long range (nonlocal) interaction between atoms located at and around the crack tip. This deviation from LEFM due to nonlocal effect at the crack tip manifests itself through (a) a finite magnitude “peak stress” near the crack tip in contrast to a singular stress field predicted by LEFM, and (b) significant non-zero tractions on the crack faces due to nonlocal effects. Eringen et al. [26] were among the first to modify continuum-based LEFM equations by employing an integral form of the stress-strain constitutive law and deriving non-singular stress fields for an isotropic solid undergoing Mode I fracture with appropriate non-local boundary conditions. The kernel function used in the nonlocal derivation enabled the introduction of a characteristic length scale into the problem, such as inter-atomic distance, which is absent in LEFM. Allegri et al [27] extended the derivation to include mode-mix and orthotropic material behavior and showed that the magnitude and the location of the peak stress near the crack tip depended on the degree of anisotropy.

### **2.3 Atomistic J-integral**

The use of J-integral [28] as a fracture criterion for inelastic materials at the macro-scale can be found extensively in the literature [29-30]. Researchers have attempted to extend the application of the J-integral to nanostructured materials [12,18,31,32], given the need for a suitable metric to quantify debonding along material interfaces at the nanoscale (e.g. grain boundary decohesion, dislocation, debonding between CNT and polymer matrix, etc.). Eshelby [33] demonstrated that the J-integral could be interpreted as the divergence of the Eshelby Energy-Momentum tensor. Further, Eshelby demonstrated that at finite temperatures, the proper energy potential for computing the J-integral depends on the thermodynamic process or ensemble. To quote Eshelby on this subject [33] “What we have called elastic energy is, more precisely, internal energy under adiabatic conditions and Helmholtz free energy under isothermal

conditions”, given that Helmholtz free energy  $\Psi = U - T\eta$  where  $U$  is internal energy,  $\eta$  is the entropy density, and  $T$  is the temperature in Kelvin. Consequently, from the basic definition of free energy, the Helmholtz free energy is the proper potential for computing  $J$  at finite temperatures for an isothermal process as it includes the entropic contribution [36]. Because free energy is complex to compute directly since it inherently involves computation of entropy density, it is not surprising that most attempts at estimating atomistic  $J$ -integral to date were performed at near zero temperatures [12, 13, 31, 34, 35], where differences between the internal energy and Helmholtz free energy are insignificant. Jones et al. [31] developed a novel MD-based methodology for computing the  $J$ -integral in nanostructured materials through the construction of continuum fields from discrete atomic data using Hardy’s [36] localization functions. These continuum fields were subsequently used to compute contour-integral expression for  $J$  that involves gradients of continuum fields, such as, the deformation gradient tensor. Nakatani et al. [37] employed changes in potential energy density in an MD simulation to estimate strain energy density. Because their system cannot be clearly determined to be isothermal or adiabatic, the relevant stress potential metric is unclear. Xu et al. [38] used a system energy release rate approach to compute critical value of  $J$  for ductile fracture of a Nano-sized crystal of nickel. Their analysis computes  $J$ -integral using changes in potential energy due to crack growth without entropic effects, even though the process takes place isothermally at a temperature of 300 K. Latapie et al. [39] use a similar MD approach to examine ductile fracture behaviour of nanosized crystals of iron (Fe) at elevated temperatures of 100, 300, and 600 K. None of these past attempts at computing fracture energy at finite temperatures have made use of the energetic and entropic contribution, except for work by Jones et al. [18], which obtained  $J$ -integral at elevated temperature using Helmholtz free energy for a Lennard-Jones model of a

perfect gold (Au) crystal. However, the results presented by Jones et. al. lack thermodynamic consistency because of negative global entropy production below a certain critical temperature ( $\sim 12$  K) for uniaxial and biaxial stretch., which is physically inadmissible.

## CHAPTER 3

### MOLECULAR DYNAMICS SIMULATIONS

#### 3.1 Introduction

Molecular dynamics (MD) is a technique based on Newtonian mechanics for computation of physical and chemical interactions of atoms and molecules. The method was originally conceived by theoretical physicists in the late 1950s (Alder and Wainwright) to study the interactions of hard spheres. In 1960s, the method was applied for simulating liquid argon and subsequently for simulating water. Then, it emerged as one of the primary tools for investigation of biological systems in the 1970s, with MD being used to simulate proteins for pharmaceutical applications. Molecular dynamics today finds application in numerous fields with its efficient ability to simulate nano-scale interactions, including, but not limited to systems pertaining to studies of, physics, material science and biology. The process involves numerically solving the Newton's equations of motion for an N-particles system. For an N atom, molecular system we have the equation of motion of atom  $i$  at time  $t$  as,

$$m_i \ddot{x}_i = - \frac{\partial V(x_1^t, x_2^t, \dots, x_N^t)}{\partial \mathbf{x}_i} \equiv \mathbf{F}_i^t \quad (i = 1, 2, \dots, N) \quad (3.1)$$

In MD, the atomistic configuration at an initial time is fed into the algorithm, along with the required force fields chosen to mathematically define the various atomic interactions. The internal force  $F_i$  at any atom  $i$  (of mass  $m_i$  and position  $x_i$ ), is computed from the energy potential ( $V$ ) chosen by the user as shown in Eq. (3.1). This chapter reviews the molecular dynamics

theory, important parameters and concepts. A discussion of the open-source MD software used, Large scale Atomic/Molecular Massively Parallel Simulator (LAMMPS) [40], and a visualization software called Open Visualization Tool (OVITO) [41] will be presented.

### 3.2 Molecular Dynamics Simulation Procedure

MD is a method of simulating interactions between atoms and molecules at nano-scale without recourse to detailed and costly quantum mechanical (*ab-initio*) calculations. A typical MD simulation is illustrated in the flowchart shown in Figure 3.1. The initial positions and velocities of individual atoms are supplied in a data file which can be read through an input script. Depending on the type of molecular system, the data file may consist of other information like force field parameters; bond, angle and dihedral information etc. The initial system is in its energy-minimized state. If it is finite temperature simulation (i.e.,  $T > 0K$ ), initial velocities are assigned to the atoms.

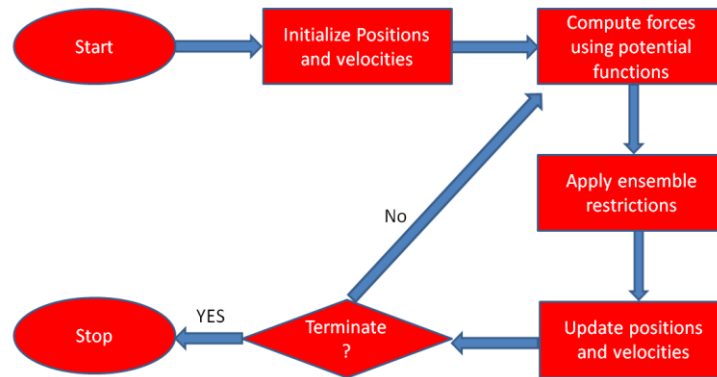


**Figure 3.1:** Flowchart of a MD process

Deformations, if any, are applied. Temperature and pressure are maintained using appropriate thermostat and barostat respectively. Using the formula given by Eq. (3.1), forces of each atom at any time  $t$  are calculated as derivatives of the potential function. Newton's second law is used to compute accelerations of the atoms. Various numerical integration schemes are

then used to determine the updated positions of each atom at the next timestep. This process is repeated until the termination condition is reached. Output data files can be generated at specific time intervals and can be analyzed. A brief discussion of each aspect of MD simulation is presented in the following sections.

### **3.3 Numerical Integration Algorithms**

Due to the complicated nature of the potential functions, it is not feasible to solve the equations of motion analytically. Thus, numerical time-integration is used to determine the updated positions and velocities of individual atoms in an MD system. Various numerical integration algorithms are available. The following criteria should be considered while choosing an algorithm:

- a) Conservation of energy and momentum is necessary;
- b) Computational efficiency must be prominent;
- c) Integration timestep should be long enough;
- d) The approximations should be reasonable enough showing minimum deviations from classical trajectories

The basic assumption in all integration algorithms is that the positions, velocities and accelerations can be approximated by a Taylor series expansion. Some of the integration algorithms are discussed here.

#### **3.3.1 Verlet Algorithms**

Application of Verlet algorithm in molecular dynamics was popularized in the 1960s

[42]. This method uses the positions ' $r$ ' and accelerations of the atoms at time ' $t$ ' along with the positions at time ' $t - \Delta t$ ' in order to calculate the new position at time ' $t + \Delta t$ '. Using Taylor series expansion, position at time ' $t + \Delta t$ ' and ' $t - \Delta t$ ' can be written as,

$$r(t + \Delta t) = r(t) + v(t)\Delta t + \frac{1}{2}a(t)\Delta t^2$$

$$r(t - \Delta t) = r(t) - v(t)\Delta t + \frac{1}{2}a(t)\Delta t^2 \quad (3.2)$$

where,  $v$  is the velocity and  $a$  is the acceleration. Taking a sum of the two equations, the updated position in terms of previous position and accelerations can be written as,

$$r(t + \Delta t) = 2r(t) - r(t - \Delta t) + a(t)\Delta t^2 \quad (3.3)$$

It is evident from the equation that explicit computation of velocities is not required. While it is simple to implement and computation resource friendly, this method is not very accurate.

### 3.3.2 Leap-frog Algorithm

Some of the shortcomings of the Verlet algorithm can be overcome by using the leap-frog algorithm [43]. It involves explicit computation of midstep velocities ' $v$ ' at time  $t + 0.5\Delta t$  is given by (3.4)

$$v(t + 0.5\Delta t) = v(t - 0.5\Delta t) + a(t)\Delta t \quad (3.4)$$

The positions ' $r$ ' and velocity ' $v$ ' at time  $t + \Delta t$  can then be computed as

$$r(t + \Delta t) = r(t) + v(t + 0.5\Delta t)\Delta t$$

$$v(t) = 0.5(v(t - 0.5\Delta t) + v(t + 0.5\Delta t)) \quad (3.5)$$

The velocities leap over the positions and the positions in turn leap over the velocities and hence the name of the algorithm. Though this method has the advantage of explicit computation of velocities, the positions and velocities are calculated at the different times.

### 3.3.3 Beeman's Algorithm

A variant of the Verlet algorithm, Beeman's algorithm [44] produces positions identical to the Verlet method but used a different formula for velocities. In this method, the velocities 'v' and positions 'r' are given by the following expressions

$$v(t + \Delta t) = v(t) + 1.5a(t)\Delta t - 0.167a(t - \Delta t)\Delta t$$

$$r(t + \Delta t) = r(t) + v(t)\Delta t + 0.5a(t)\Delta t^2 \quad (3.6)$$

Along with a better energy conservation, this method produces a more accurate expression for velocities. The downside is the computational expense because of the increased complexity of the expressions.

### 3.3.4 Velocity Verlet Algorithm

One of the more commonly used numerical integration methods used in MD simulations is the velocity Verlet algorithm [45]. As the name indicates, it is a variation of the Verlet algorithm discussed earlier. In this method, the velocities 'v' and positions 'r' at time  $t + \Delta t$  are given by,

$$v(t + \Delta t) = v(t) + 0.5(a(t) + a(t + \Delta t))\Delta t$$

$$r(t + \Delta t) = r(t) + v(t)\Delta t + 0.5a(t)\Delta t^2 \quad (3.7)$$

This algorithm produces updated positions and velocities of the atoms without compromising on the precision, which occurs in the original Verlet method. The velocity Verlet algorithm has been implemented in LAMMPS [46] and is used in this thesis. More discussion on LAMMPS will be presented in a different section.

### 3.4 Thermostats

Temperature plays a vital role in MD simulations. For finite temperature simulations, it is important that the desired value is maintained as closely as possible by using a thermostat facilitates this. This section presents a discussion of the various types of thermostats available. From statistical mechanics, temperature of a system of atoms is defined as the average of kinetic energies of all particles. Considering the kinetic energy of the system is  $K$ , the temperature  $T$  of an  $N$  atom system can be given as,

$$T = \frac{2 \langle K \rangle}{3 N k_B} \quad (3.8)$$

where,  $k_B$  is Boltzmann's constant, and the angular brackets imply average over an ensemble. It is not possible to keep the temperature at a fixed value during the simulation due to the random fluctuations in velocities. Therefore, only the average value of temperature can be maintained at a constant value during simulations. As given by Eq. (3.8), the temperature of a system depends only on the kinetic energy of the atoms, which in turn depends on the random velocities of atoms in the system. Velocities scaling can hence be used to control the temperature of a system, which can be achieved using a thermostat. Some of the commonly used thermostats are discussed below.

### **3.4.1 Anderson Thermostats**

In Anderson thermostat, the system is coupled to a heat bath using stochastic forces which modify the kinetic energy of the atoms in the system [47]. The time between the collisions is decided randomly. When a collision event occurs, the velocity of the selected particle is replaced by a value chosen from a random Boltzmann distribution for that specified temperature.

### **3.4.2 Berendson Thermostats**

Berendson thermostat is another way to rescale the velocities of the atoms in the system to provide a temperature control during molecular dynamics simulations [48]. In this method, the heat bath at the desired temperature is coupled with the MD system. Any changes in the kinetic energy of the system are suppressed by this thermostat and thus, temperature control is achieved. This thermostat is suitable for larger systems and due to its computational efficiency, it is widely used.

### **3.4.3 Nose-Hoover Thermostats**

The Nose-Hoover thermostat is considered to be one of the most accurate and computationally efficient method for temperature control in an MD simulation. Originally developed by Nose [49], and subsequently improved by Hoover [50], it is a deterministic scheme for constant temperature simulations. The heat bath is considered as an integral part of the system by adding an artificial variable ' $s$ ' with an associated mass ' $Q$ ' and a velocity ' $s$ '. The extent of coupling between the heat bath and the MD system is determined by the magnitude of ' $Q$ '. The simulations reported in this dissertation employ this thermostat for maintaining the

desired temperature.

### 3.5 Barostats

Most laboratory experiments are conducted at constant temperature and pressure. Hence, as with temperature, it is important to maintain proper pressure control during MD simulations. Berendsen barostat [51] and Anderson barostat [52] are two commonly used barostats to control pressure in MD simulations. In order to maintain the desired system pressure, the dimensions of the simulation box are dynamically adjusted.

### 3.6 Ensembles

An ensemble is a collection of all possible systems within a phase space that have different microscopic states but have an identical thermodynamic state. It is a useful way of obtaining system averages from various microscopic states that could occur. Three types of ensembles are commonly used in molecular dynamics simulations. They are NVE, NVT and NPT, where N is the number of particles (atoms) in the system, E is the total energy of the system, V is the volume of the system, T is the temperature and P is the pressure. A schematic of each of these ensembles is shown in Figure 3.2. A brief discussion of each type of ensemble follows.

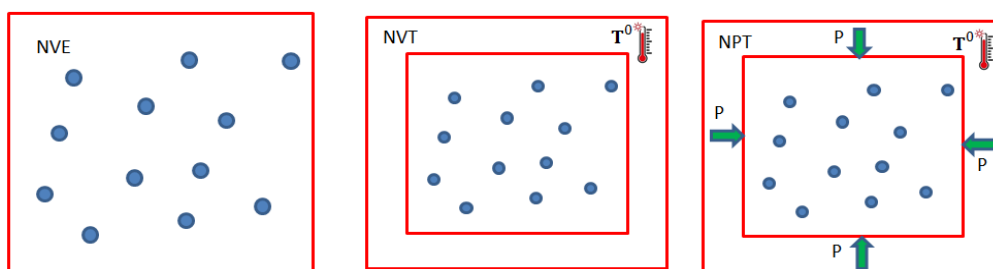


**Figure 3.2:** Ensembles

#### 3.6.1 NVE Ensemble

NVE ensemble, also known as microcanonical ensemble, is used to describe an isolated system. As the name suggests, in this ensemble, the number of particles (N), volume (V) and total energy (E) of the system remains unchanged. It usually corresponds to a process where there is no exchange of heat or particles with its surroundings.

### **3.6.2 NVT Ensemble**

NVT ensemble is also known as canonical ensemble and refers to a system where the number of particles (N), volume (V) and temperature (T) are conserved. It is also known as constant temperature molecular dynamics since the temperature of the system remains unchanged throughout the simulation. This ensemble represents a system in thermal equilibrium with a heat bath at the prescribed temperature (T). A thermostat is used to add or remove energy from the MD system. Various types of thermostats like Nose-Hoover, Berendsen, Andersen etc. are available in MD. A discussion on the types of thermostats was presented earlier.

### **3.6.3 NPT Ensemble**

Also known as isothermal-isobaric ensemble, NPT corresponds to a system where the number of particles (N), pressure (P) and temperature (T) remain unchanged over time. Similar to NVT ensemble, a thermostat is required to conserve temperature of the system. In addition, a barostat is needed to conserve the pressure. Different types of barostats have been discussed earlier. This ensemble most closely resembles the laboratory experimental conditions since most experiments are conducted under constant pressure and temperature.

## **3.7 Boundary Conditions**

In order to obtain the bulk properties from MD simulations, it is important to account for

the edge effects. One way of eliminating these edge effects is to simulate an extremely large system to ensure that the surfaces and edges have only a small influence on the properties. Due to computational expenses, this method is not feasible. The use of periodic boundary conditions facilitates the simulation of an infinitely large system while being computationally efficient. The simulation box is replicated throughout space to form an infinite large system, as shown in Figure 3.3 [53]. During the simulation, when the position of a particle in one box is updated, this change is replicated on that particle in all the boxes. Any edge effects are thus eliminated because when a particle leaves one box, an identical particle enters through the opposite face.

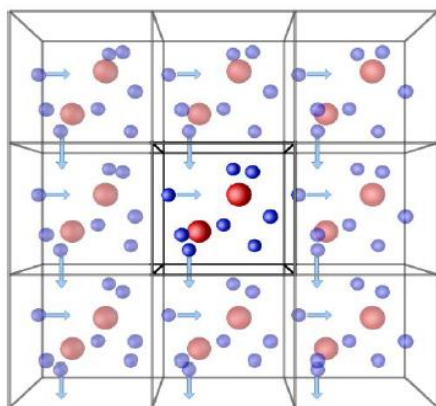


**Figure 3.3:** Schematic illustrating a 3D simulation box with Periodic Boundary Conditions in all directions

### 3.8 Potential Functions

Potential function plays a critical role in molecular dynamics simulations. Since accelerations of the atoms/particles are determined by the potential function, which in turn determine the updated velocities and positions of the atoms/particles, it is vital that the potential function is appropriately defined. Potential function is a mathematical description of the potential energy of a system of interacting particles. It characterizes the way interactions occur between all the particles in a molecular dynamics system. Quantum mechanical calculations and

experimental observations are used to obtain the parameters in a potential function. Various potential functions can be defined to simulate various molecular systems such as biological, chemical, etc. The type of molecular system being used in a particular simulation dictates the exact functional form and parameters of the potential function.

Quantum mechanics (QM) based methods provide a better description of the interactions in a system with many particles. However, doing purely QM based calculations on a large system becomes computationally unfeasible. In order to reduce the fully quantum descriptions to a potential function description involves the Born-Oppenheimer approximation, which allows the energy of the system to be written as a product of mutually independent functions of nuclear and electron coordinates [54]. Additionally, the nuclei of the atoms could be treated as point particles which follow Newtonian dynamics. In MD, the position and configuration of electrons within the shell of atoms are ignored and focus is entirely on the energy due to the position of nuclei with respect to each other. This facilitates the use of MD to simulate large molecular systems. The molecular force fields employed in MD algorithm are in general empirical fits to quantum mechanical calculations. In certain cases, the molecular dynamics algorithm is able to provide results as good as the highest quantum mechanical calculations, for a fraction of computer time [54].

The potential functions play a critical role in molecular dynamics simulations. Defining the correct potential function is very crucial since, the potential functions determine the acceleration of the atoms or particles, which is then used to update the positions and the velocities of all the atoms or particles in the system. There are many force fields available in literature, resourceful for simulating various types of systems. Traditionally, force fields with fixed bond topologies were used to model covalent systems by defining the bonds at the

beginning of the simulation and remain fixed throughout. Some of the common force fields used in such methodologies are, AMBER, OPLS, CHARM and COMPASS. The MD systems modeled using such force fields with their corresponding assumptions have been analyzed and proven to be appropriate for systems like polymers and proteins. However, these force fields are not adaptable to reactive systems, and they are not able to replicate the bond breakage and/or bond formation reactions in the MD system. So, to overcome this, reactive force fields are suggested to be used for material research, which allows us to study crack-formation, propagation and fracture. Reax Force Field (ReaxFF) is a reactive force field based on the bond order, developed by Adri van Duin et al. [55]. In this thesis, a bond order based potential function called Reactive Force Field (ReaxFF) is used.

### **3.8.1 Reactive Force Field (ReaxFF)**

Traditional potential functions like OPLS are much simpler to use and are computational friendly, but they are unable to simulate chemical reactions since they lack the capability to simulate bond formation and bond breakage between the atoms. However, more recent potential functions like Reactive force field (ReaxFF), which is a bond order-based force field, allows continuous bond breakage and formation [55], and suits more closely to simulate material behavior under sustained loading. This advantage is used to serve the purpose of this dissertation more relevantly. ReaxFF uses the bond distance-bond order relationship on one hand and the bond order-bond energy relationship on the other, to simulate the proper dissociation of bonds to separated atoms. Valence terms like angle and torsion, present in the force field are also defined in terms of the same bond orders, which when the bonds break, goes to zero. Non-bonded interactions between the atoms, like van der Waals and Coulombic potentials, are also taken into consideration in the ReaxFF force field, thereby incorporating all the interactions presents in the

system. The ReaxFF parameters are derived from quantum chemical calculations on bond dissociation, reactions of small molecules, heat formation and geometry data of several stable hydrocarbon compounds.

Similar to the empirical force fields like OPLS, the total energy of the system is described by ReaxFF as a sum of various partial energies as shown in Equation (3.9)

$$E_{\text{system}} = E_{\text{bond}} + E_{\text{over}} + E_{\text{angle}} + E_{\text{tors}} + E_{\text{vdWaals}} + E_{\text{coulomb}} + E_{\text{specific}} \quad (3.9)$$

Each of these partial energy terms is a function of bond order, which depends on the interatomic distance. The dependency of Bond Order between two atoms  $i$  and  $j$ , to the interatomic distance between them, can be described as:

$$BO_{ij} = \exp\left(p_{bo1} \left(\frac{r_{ij}}{r_0}\right)^{p_{bo2}}\right) + \exp\left(p_{bo3} \left(\frac{r_{ij}}{r_0}\right)^{p_{bo5}}\right) + \exp\left(p_{bo5} \left(\frac{r_{ij}}{r_0}\right)^{p_{bo6}}\right) \quad (3.10)$$

Here,  $r_{ij}$  is interatomic distance,  $r_0$  is equilibrium bond length and the  $p_{be}$  terms are empirical parameters obtained from fitting DFT computation. Bond-order has a value between zero and one. It is evident that as the bond order goes to zero between two adjacent atoms, the energy of the covalent bond will also reduce to zero and the bond is about to break.

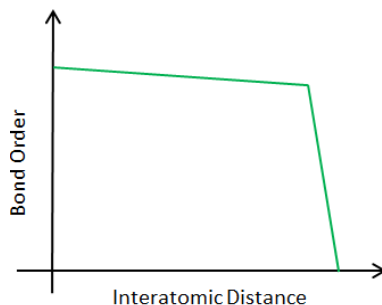


**Figure 3.4:** Schematic plot between Bond Order and Interatomic Distance

Once the bond order is computed, all the partial energies are determined. For example,

the bond energies can be computed using the formula given by,

$$E_{ij} = -D_e (BO_{ij}) \exp\left(p_{be,1} \left(1 - BO_{ij}^{p_{be,2}}\right)\right) \quad (3.11)$$

where,  $BO_{ij}$  is the bond order for atoms  $i$  and  $j$ ,  $D_e$  and  $p_{be,1}$  are the bond parameters. All the other partial energies can be calculated using similar formulae based on bond order. Since interatomic distance is the only parameter governing all the energies, keeping track of bond order facilitates dynamic formation and breakage of chemical bonds. This attribute is extremely effective in simulating initiation and propagation of nanoscale cracks. One of the downsides of using ReaxFF compared to OPLS is the need for increased computational resources.

### 3.9 Overview of LAMMPS

The molecular dynamics simulations for this research have been performed using LAMMPS. It stands for large-scale atomic/molecular massively parallel simulator. LAMMPS is a free and open source software maintained by Sandia National Laboratories. It is a classical molecular dynamics code designed for simulating molecular and atomic systems on parallel computers using spatial-decomposition techniques. It can be used to model atoms or, more generically, as a parallel particle simulator at the atomic, meso, or continuum scale. LAMMPS is highly portable and can be run on a single processor or in parallel. LAMMPS runs from an input script. The input file starts with definitions of atoms, units and boundary conditions. A number of atom types are supported in LAMMPS like atoms, coarse-grain particles, metals, granular materials and more. Different unit systems, such as LJ, real, metal etc. are available in LAMMPS. The actual units of the physical quantities are dictated by the unit system defined in the input script. For example, time is measured in femtoseconds in real system while it is

measured in picoseconds according to the metal unit system. Boundary conditions can be chosen to be either periodic or non-periodic.

Atomistic data is read from a data file. The data file consists of co-ordinates, bonds, angles and dihedral information for all atoms. Appropriate potential field coefficients, simulation parameters are also defined in the input file. LAMMPS supports numerous potential functions, including OPLS and ReaxFF used in this dissertation. Other parameters like temperature can also be defined along with appropriate ensemble conditions like NVE, NPT or NVT. The atoms in the MD system are contained in a simulation box. Any deformation applied to the box is transferred to the system of atoms. The deformation parameters are defined in the input file. LAMMPS allows to calculate time and spatial averages of physical quantities, such as temperature, pressure, energies, etc. The time-step and number of steps are also specified in the input file. Desired output parameters can be stored in separate text files at specified time-step intervals. LAMMPS has no inherent way of graphically analyzing the output files and so another tool called OVITO is used for that purpose.

### **3.10 Open Visualization Tool (OVITO)**

In order to translate the raw output data from LAMMPS, Open Visualization Tool (OVITO) was used. It is a free, open source visualization and analysis software which can be used on all major operating systems. It was originally developed by Alexander Stukowski at Darmstadt University of Technology in Germany [41]. Apart from the ease of use, some of the other advantages of OVITO include support for multiple file formats, diverse analysis tools like color coding of atoms, slicing, bond analysis etc. The visualizations created in OVITO can be exported as high quality images and animations.

## CHAPTER 4

### THEORETICAL BACKGROUND

#### 4.1 Flaw Size Insensitivity

Postulating the existence of stress singularity at a crack tip in a material continuum, linear elastic fracture mechanics (LEFM) proposes a material property termed fracture toughness (i.e.,  $K_{Ic}$  or  $G_{Ic}$ ) to determine whether a brittle solid loses its load-carrying capability due to crack initiation and propagation. If there is a macroscale central crack in an finite width plate is subjected to remote uniform tension, the critical far-field stress required to initiate fracture,  $\sigma_{cr}$ , as a function of crack length,  $2a$ , can be estimated by,

$$\sigma_{cr, far-field} = \sqrt{\frac{2\beta E\gamma}{\pi a}} \quad (1)$$

where,  $E$  is the Young's modulus,  $\gamma$  is the energy required per unit area to create a new fracture surface,  $\beta$  is a finite geometry correction factor, and  $w$  is the width of the plate. According to Eqn. (1), on the basis of fracture energy as a material constant, once the crack length,  $2a$ , approaches nanoscale, the far-field critical stress ( $\sigma_{cr}$ ) could exceed the theoretical strength ( $\sigma_{th}$ ) of a perfect solid. Because this is

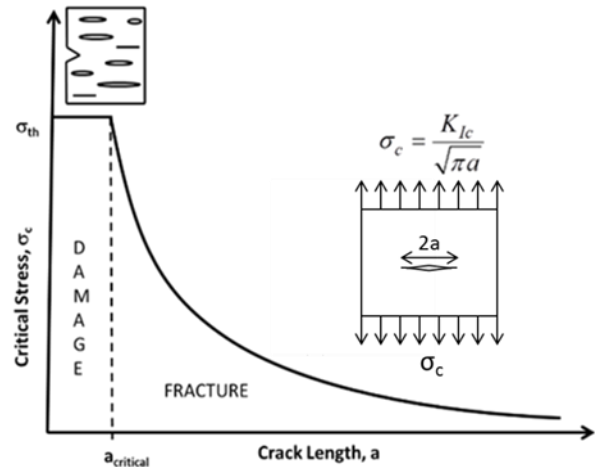


**Figure 4.1:** Crack length effect at the nanoscale leading to a brittle to ductile transition

not physically admissible, the critical crack length can be calculated as [16,56],  $a_{cr} = \frac{2\beta E\gamma}{\pi\sigma_{th}^2}$ ,

which is the crack length below which the strength of nanoscale structures is governed by the theoretical strength and not by fracture energy, thereby triggering a brittle fracture to strength-based transition in the failure mode as schematically depicted in Fig. 1. For a centre-cracked graphene sheet of width  $w = 30$  nm, assuming a Young's modulus  $E = 471$  GPa, surface energy  $\gamma = 5.9$  J/m<sup>2</sup> and theoretical strength  $\sigma_{th} = 115$  GPa, the critical half-crack length,  $a_{cr}$ , is calculated to be 0.1338 nm (1.338 Å) for  $\beta = 0.99$ . Consequently, flaw-size insensitivity in a graphene sheet will only become evident for flaw sizes at or below 0.27 nm (2.7 Å), which is very small even by the standard of atomistic scale. However, for epoxy polymer, the critical crack length is calculated to be around 2560 nm or 2.5 microns, which is quite large from atomistic modelling viewpoint.

#### 4.2 Effect of non-locality in nanoscale

While the above brittle to ductile transition and resulting flaw-size tolerance is postulated based on purely continuum mechanics considerations, there is an additional nanoscale rationale for deviation from LEFM. As pointed out by several researchers, nonlocal interactions can give rise to a non-singular stress field near the crack tip leading to a strength-based failure criterion for isotropic [26] and for orthotropic materials [27]. They have shown evolution of finite stresses at the crack tip in nonlocal orthotropic continua for all the three fracture modes of fracture. They have also shown the existence of non-zero self-balanced tractions on the crack edges for both isotropic and orthotropic continua. Because atomistic simulations are inherently non-local, it is likely that the resulting non-zero tractions along the crack face and finite stress concentration ahead of the crack-tip would lead to anomalous fracture behaviour deviating from the Griffith

theory.

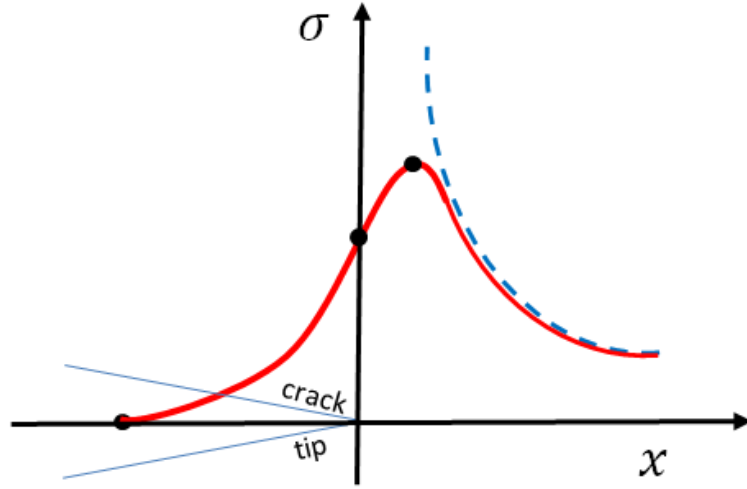


**Figure 4.2:** Nonlocal effect at nanoscale

### 4.3 Quantized Fracture Mechanics

Consider the fracture of a crystalline nanoscale linear elastic infinite plate in tension with a uniform thickness  $t$ , lattice spacing of  $a$ , crack tip radius  $\rho$ , and with a crack of length  $2l$  orthogonal to the applied far-field (Mode I) stress. The failure of the material is described by the fracture toughness and the critical far field stress at failure by the fracture quantum at the atomistic length-scale [10]

$$\sigma_{f-QFM} = K_{IC} \sqrt{\frac{1 + \rho/2a}{\pi(l + a/2)}} = K_{IC} \sqrt{\frac{1 + \rho/2a}{\pi a(n+1)/2}} \quad (4.3)$$

The implication here is that the flaw length,  $2l$ , can only grow in discrete increments of the lattice spacing  $a$ , and hence can only be an integer function of  $a$ , that is,  $2l = na$ . Therefore, Eqn. (4.3) mandates that the QFM based far-field critical stress is allowed to have certain discrete values corresponding to  $n = 1, 2, 3$  etc., with forbidden bands in between. Of course, when  $2l/a$  is large, and  $n$  tends to infinity, then QFM reverts to conventional continuum fracture

mechanics. By tracking the bond order at the crack tip and computing the critical value of J-integral at the crack tip at successive bond breakage during crack growth, atomistic J-integral should be able to provide clear evidence for the quantized fracture effect as discussed later in this paper. In this context, our proposed approach is more robust and accurate than the approach employed by Dewapriya et al [12] using J-integral, because they assumed that carbon-carbon bond breakage in an armchair graphene sheet occurs at 15% strain and did not use the reduction of bond order to zero to ensure bond separation.

#### 4.4 Different modes of fracture and their continuum quantification

Fracture can be defined as the separation of a structure into two or more pieces when subjected to mechanical loading. It is associated with the development of a displacement discontinuity in the structure followed by crack growth. When the direction of loading is perpendicular to the direction of crack growth, it is called mode I fracture (see Figure 4.3), which will be the fracture mode studied in this research.

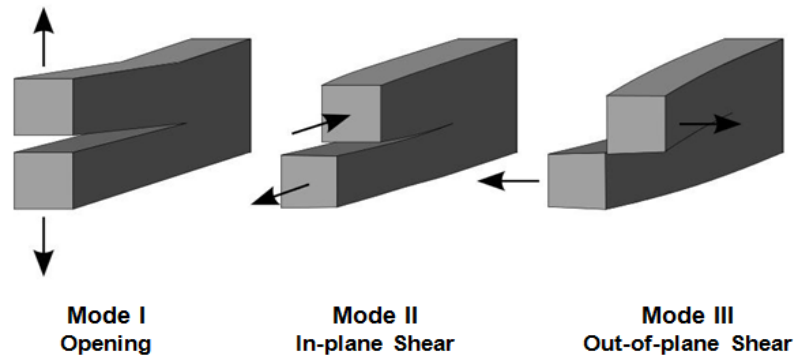


**Figure 4.3:** Three modes of fracture

Fracture can be characterized through parameters such as strain energy release rate ( $G$ ), stress intensity factor ( $K$ ), and the J-integral ( $J$ ). The critical values of these parameters represent the fracture strength of a material. Once the critical value is reached, crack initiation occurs in

the material. While  $G$  and  $K$  are widely used to characterize fracture, they are applicable only in the linear elastic range of the stress-strain response of the material. On the other hand, J-integral is identical to  $G$  in the linear range but has the advantage of being applicable in the nonlinear range as well as being contour path independent. Also, the critical value of J-integral at crack initiation is directly related to fracture toughness of the material, while the value of J as a function of crack length during crack growth provides the resistance of the material to crack growth, or R-curve. The applicability of J-integral for characterizing fracture is discussed in Chapter 2. Based on these advantages, J-integral was used as fracture criterion at the nanoscale in this research.

#### 4.5 J-integral and its atomistic evaluation methodology

This study employs MD simulations to compute atomistic J-integral, in order to quantify the influence of nano-fillers (such as graphene platelets) on fracture toughness of a polymer. The concept of J-integral was developed by J R Rice [28]. In conventional macro-scale fracture mechanics, the total J-integral vector ( $J_T$ ), defined as the divergence of the Eshelby energy-momentum tensor [33] (as shown in Eq. (4.4)), has been used to quantify the crack driving force available from thermo-mechanical loading as well as material inhomogeneities.

$$\mathbf{J}_T = \int_{\partial\Omega} \langle \underline{S} \rangle N dA = \int_{\partial\Omega} (\langle \Psi \rangle N - \langle \underline{H}^T \underline{P} \rangle N) dA = J_U - J_\eta \quad (4.4)$$

In Eq. (4.4),  $\underline{S}$  is the Eshelby energy-momentum tensor,  $\Psi$  is the free energy density,  $\underline{H}$  is the displacement gradient tensor,  $\underline{P}$  is the first Piola-Kirchhoff stress tensor,  $N$  is the outward normal to the surface  $\partial\Omega$  along which contour the J-integral is being evaluated,  $J_U$  is the contribution to J-integral due to internal energy ( $U$ ), and  $J_\eta$  is the entropic contribution ( $J_U$  and  $J_\eta$  will be discussed in detail in following sections). Here it is assumed that ensemble average  $\langle * \rangle$  is

approximated by the time average of the quantity over a sufficiently long period of time. The critical value of scalar component  $J_k$  at crack initiation is related to the fracture toughness of the material, where the subscript  $k$  denotes Cartesian components of the J vector ( $k=1, 2, 3$ ) in three-dimensions and these components are related to but are not the same as the three primary fracture modes. Specifically,  $J_1 = J^I + J^{II} + J^{III}$  and  $J_2 = -2\sqrt{(J^I J^{II})}$ , where subscripts imply Cartesian components of the J-vector, and the superscripts imply standard fracture modes [57]. In the absence of Mode III, i.e., for purely in-plane deformation, the above equations can be solved to obtain the individual fracture modes from the cartesian components of the J vector as given by,

$$J^I = \frac{J_1 \pm \sqrt{J_1^2 - J_2^2}}{2}, \text{ and } J^{II} = J_1 - J^I. \text{ Therefore, the Cartesian components of the J-integral}$$

can be used as a suitable metric for estimating the crack driving force as well as the fracture toughness of a material as the crack begins to initiate, for Mode I, Mode II and for mixed mode fracture processes undergoing proportional loading. However, for the conventional macroscale definition of the J-integral to be valid at the nanoscale in terms of the continuum stress and displacement fields (and their spatial derivatives) requires the construction of local continuum fields from discrete atomistic data and

using these data in the conventional contour integral expression for J, as given by Eq. (4.4) [18,33]. One such methodology was proposed by Hardy [36], that allows for the local averaging necessary to obtain the definition of free energy, deformation gradient, and Piola-

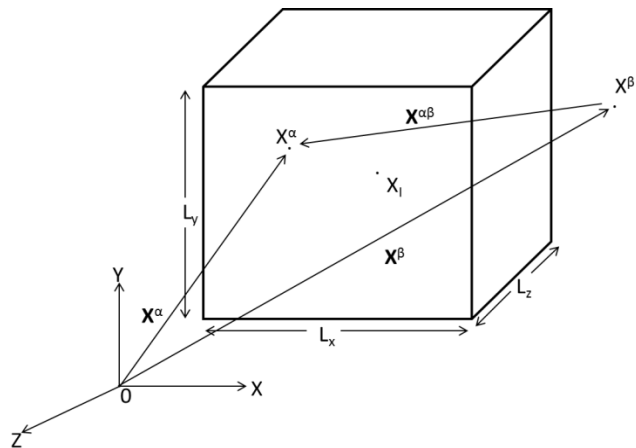


**Figure 4.4:** Illustration of a localization box with atom  $\alpha$  inside and atom  $\beta$  outside the box

Kirchoff stress as fields (and divergence of fields) and not just as total system averages. The formulae used for evaluating each term on the R.H.S. in Eq. (4.4) from MD simulations are given below. The energetic component of total J ( $J_U$ ) is computed using the formula,

$$\mathbf{J}_U = \int_{\partial\Omega} (\langle \mathbf{U} \rangle \mathbf{N} - \langle \underline{\mathbf{H}}^T \underline{\mathbf{P}} \rangle \mathbf{N}) dA \quad (4.5)$$

In order to facilitate J-integral computation using discrete atomistic data, localization boxes (as shown in Figure 4.4) are constructed along the integral contour the position of an atom with respect to the box determined the value of localization function. The localization function has to satisfy the following conditions:  $\psi > 0$  and  $\int_{\Omega} \psi dV = 1$ . The localization function used in this work is given by Eq. (4.6).

$$\zeta(\mathbf{X} - \mathbf{X}^\alpha) = \begin{cases} \frac{1}{L_x L_y L_z} \text{ if } \begin{cases} X_I - \frac{L_x}{2} \leq X^\alpha \leq X_I + \frac{L_x}{2} \\ Y_I - \frac{L_y}{2} \leq Y^\alpha \leq Y_I + \frac{L_y}{2} \\ Z_I - \frac{L_z}{2} \leq Z^\alpha \leq Z_I + \frac{L_z}{2} \end{cases} \\ 0 \end{cases} \quad (4.6)$$

where,  $L_x$ ,  $L_y$  and  $L_z$  are the dimensions of the localization box and  $X_I$ ,  $Y_I$  and  $Z_I$  are the coordinates of the centroid, as illustrated in Figure 2. The terms required for computation of  $J_U$  can now be defined as,

$$U(\mathbf{X}, t) = \sum_{I=1}^K \sum_{\alpha=1}^M N_I(\mathbf{X}) \zeta_{I\alpha}(\mathbf{X}^\alpha - \mathbf{X}_I) \phi^\alpha(t) - U_R(\mathbf{X}) \quad (4.7)$$

$$\underline{\mathbf{H}}(\mathbf{X}, t) = \nabla_x \mathbf{u}(\mathbf{X}, t) = \sum_{I=1}^K \sum_{\alpha=1}^M \nabla_x N_I(\mathbf{X}) \zeta_{I\alpha}(\mathbf{X}^\alpha - \mathbf{X}_I) \mathbf{u}^\alpha(t) \quad (4.8)$$

$$\underline{P}(\mathbf{X}, t) = -\frac{1}{2} \sum_{\alpha=1}^M \sum_{\beta \neq \alpha}^M f^{\alpha\beta} \otimes \mathbf{X}^{\alpha\beta} B^{\alpha\beta}(\mathbf{X}) \quad (4.9)$$

In Eq. (4.7),  $\phi^\alpha$  is atomistic potential of atom  $\alpha$ ,  $U_R(\mathbf{X})$  is the reference potential energy density of atom  $\alpha$  at 0 K,  $\zeta$  is the Hardy localization function,  $M$  is the number of atoms in the localization box and  $N_I(\mathbf{X})$  are interpolation functions, with  $I=1, K$ , where  $K$  is the total number of nodes. In Eq. (4.8),  $\mathbf{u}(\mathbf{X}, t)$  is the displacement vector. In Eq. (4.9),  $f^{\alpha\beta}$  is the vector representing the force between atoms  $\alpha$  and  $\beta$ ,  $\mathbf{X}^{\alpha\beta}$  is the vector representing the difference in their positions, and  $B^{\alpha\beta}$  is the bond function defined by Hardy [36]. Detailed derivation of Eq. (4.7), Eq. (4.8) and Eq. (4.9) follows.

#### 4.5.1 Evaluation of energy density field (U):

$$U(\mathbf{X}, t) = \sum_{\alpha=1}^M \left( \phi^\alpha(t) - \phi_X^\alpha \right) \zeta(\mathbf{X} - \mathbf{X}^\alpha) \quad (4.10)$$

$$U(\mathbf{X}, t) = \sum_{\alpha=1}^M \phi^\alpha(t) \zeta(\mathbf{X} - \mathbf{X}^\alpha) - U_R(\mathbf{X}) \quad (4.11)$$

where,  $\phi^\alpha$  is atomistic potential,  $\phi_X^\alpha$  is the reference potential energy density of at 0 K,  $\zeta$  is the localization function,  $U_R(\mathbf{X})$  is the reference potential energy density of atom  $\alpha$  at 0 K.

Defining,

$$\phi_I(\mathbf{X}_I, t) = \sum_{\alpha=1}^M \zeta_{I\alpha}(\mathbf{X}^\alpha - \mathbf{X}_I) \phi^\alpha(t) \quad (4.12)$$

$$\phi(\mathbf{X}, t) = \sum_{I=1}^K N_I(\mathbf{X}) \phi_I(\mathbf{X}_I, t) \quad (4.13)$$

where,  $N_I(\mathbf{X})$  are the interpolation functions (discussed later). Substituting (4.12) and (4.13) in (4.10),

$$U(\mathbf{X}, t) = \sum_{I=1}^K \sum_{\alpha=1}^M N_I(\mathbf{X}) \zeta_{I\alpha}(\mathbf{X}^\alpha - \mathbf{X}_I) \phi^\alpha(t) - U_R(\mathbf{X}) \quad (4.14)$$

where,  $M$  is the number of atoms in the localization box and  $N_I(\mathbf{X})$  are interpolation functions, with  $I=1, K$ , where  $K$  is the total number of nodes

#### 4.5.2 Evaluation of Displacement gradient ( $\underline{H}$ ):

$$\underline{H}(\mathbf{X}, t) = \nabla_x \mathbf{u}(\mathbf{X}, t) = \nabla_x \sum_{I=1}^K N_I(\mathbf{X}) \mathbf{u}_I(t) \quad (4.15)$$

$$\underline{H}(\mathbf{X}, t) = \sum_{I=1}^K \sum_{\alpha=1}^M \nabla_x N_I(\mathbf{X}) \zeta_{I\alpha}(\mathbf{X}^\alpha - \mathbf{X}_I) \mathbf{u}^\alpha(t) \quad (4.16)$$

where,  $\mathbf{u}(\mathbf{X}, t)$  is the displacement vector of atom  $\alpha$ ,  $M$  is the number of atoms in the localization box and  $N_I(\mathbf{X})$  are interpolation functions.

#### 4.5.3 Evaluation of First Piola-Kirchhoff Stress:

The bond function is used to account for the interatomic forces where one atom is inside the localization box and the other one is outside. In such cases, only the fraction of the bond length inside the localization box is used for force computations. The bond function can be defined as,

$$B^{\alpha\beta} = \int_0^1 \zeta \left( \lambda(\mathbf{X}_\alpha - \mathbf{X}) + (1-\lambda)(\mathbf{X}_\beta - \mathbf{X}) \right) d\lambda \quad (4.17)$$

where,  $\lambda$  goes from 0 to 1 if  $\beta$  is inside the box. Otherwise only till the fraction of  $\mathbf{X}^{\alpha\beta}$  inside the box.

Setting  $\mathbf{r} = \lambda \mathbf{X}^{\alpha\beta} + \mathbf{X}^\beta - \mathbf{X} \Rightarrow d\mathbf{r} = -d\mathbf{X}$  and taking derivative of  $\zeta(\lambda \mathbf{X}^{\alpha\beta} + \mathbf{X}^\beta - \mathbf{X})$  with respect to  $\lambda$ ,

$$\frac{\partial \zeta}{\partial \lambda} = \left( \frac{\partial \zeta}{\partial \mathbf{r}} \right) \left( \frac{\partial \mathbf{r}}{\partial \lambda} \right) = \left( -\frac{\partial \zeta}{\partial \mathbf{X}} \right) (\mathbf{X}^{\alpha\beta}) = -\mathbf{X}^{\alpha\beta} \cdot \nabla_x \zeta(\lambda \mathbf{X}^{\alpha\beta} + \mathbf{X}^\beta - \mathbf{X}) \quad (4.18)$$

Integrating the above equation with respect to  $\lambda$  from 0 to 1,

$$\int_0^1 \frac{\partial \zeta}{\partial \lambda} d\lambda = -\mathbf{X}^{\alpha\beta} \cdot \nabla_x \int_0^1 \zeta(\lambda \mathbf{X}^{\alpha\beta} + \mathbf{X}^\beta - \mathbf{X}) d\lambda \quad (4.19)$$

$$\zeta(\mathbf{X}^\alpha - \mathbf{X}) - \zeta(\mathbf{X}^\beta - \mathbf{X}) = -\mathbf{X}^{\alpha\beta} \cdot \nabla_x B^{\alpha\beta}(\mathbf{X}) \quad (4.20)$$

From the definition of momentum density,

$$\rho_0 \frac{d\mathbf{V}}{dt} = \sum_{\alpha=1}^M m^\alpha \frac{d\mathbf{V}^\alpha}{dt} \zeta(\mathbf{X}^\alpha - \mathbf{X}) = \sum_{\alpha=1}^M (\mathbf{f}^\alpha + m^\alpha \mathbf{b}^\alpha) \psi(\mathbf{X}^\alpha - \mathbf{X}) \quad (4.21)$$

From internal force term,

$$\sum_{\alpha=1}^M \mathbf{f}^\alpha \zeta(\mathbf{X}^\alpha - \mathbf{X}) = \sum_{\alpha=1}^M \sum_{\beta \neq \alpha}^M \mathbf{f}^{\alpha\beta} \zeta(\mathbf{X}^\alpha - \mathbf{X}) = \frac{1}{2} \sum_{\alpha=1}^M \sum_{\beta \neq \alpha}^M \mathbf{f}^{\alpha\beta} [\zeta(\mathbf{X}^\alpha - \mathbf{X}) - \zeta(\mathbf{X}^\beta - \mathbf{X})] \quad (4.22)$$

Substituting (4.19) & (4.20) in (4.21),

$$\rho_0 \frac{d\mathbf{V}}{dt} = \sum_{\alpha=1}^M \left\{ \frac{1}{2} \sum_{\beta \neq \alpha}^M \mathbf{f}^{\alpha\beta} [-\mathbf{X}^{\alpha\beta} \cdot \nabla_x B^{\alpha\beta}(\mathbf{X})] + m^\alpha \mathbf{b}^\alpha \zeta(\mathbf{X}^\alpha - \mathbf{X}) \right\} \quad (4.23)$$

$$\rho_0 \frac{d\mathbf{V}}{dt} = \nabla_x \cdot \left\{ -\frac{1}{2} \sum_{\alpha=1}^M \sum_{\beta \neq \alpha}^M \mathbf{f}^{\alpha\beta} \otimes \mathbf{X}^{\alpha\beta} B^{\alpha\beta}(\mathbf{X}) \right\} + \sum_{\alpha=1}^M m^\alpha \mathbf{b}^\alpha \zeta(\mathbf{X}^\alpha - \mathbf{X}) \quad (4.24)$$

From momentum balance equation,

$$\rho_0 \frac{d\mathbf{V}}{dt} = \nabla_x \cdot \underline{\underline{P}} + \rho_0 \mathbf{b} \quad (4.25)$$

Comparing (4.24) and (4.25),

$$\underline{\underline{P}}(\mathbf{X}, t) = -\frac{1}{2} \sum_{\alpha=1}^M \sum_{\beta \neq \alpha}^M \mathbf{f}^{\alpha\beta} \otimes \mathbf{X}^{\alpha\beta} B^{\alpha\beta}(\mathbf{X}) \quad (4.26)$$

The expression for bond function is defined as follows. Considering a localization box as shown in Figure 4.5 with one atom ( $\alpha$ ) inside the box and another atom ( $\beta$ ) outside the box.

To scale the influence of the atom outside the box, a new position of atom  $\beta$  is determined as,

$$\text{If } X_1^\beta \geq X_1^I + \frac{L_X}{2} \text{ then } X_1^{\beta N} = X_1^I + \frac{L_X}{2} \text{ else } X_1^{\beta N} = X_1^\beta$$

$$\text{If } X_1^\beta \leq X_1^I - \frac{L_X}{2} \text{ then } X_1^{\beta N} = X_1^I - \frac{L_X}{2} \text{ else } X_1^{\beta N} = X_1^\beta$$

$$\text{If } X_2^\beta \geq X_2^I + \frac{L_Y}{2} \text{ then } X_2^{\beta N} = X_2^I + \frac{L_Y}{2} \text{ else } X_2^{\beta N} = X_2^\beta$$

$$\text{If } X_2^\beta \leq X_2^I - \frac{L_Y}{2} \text{ then } X_2^{\beta N} = X_2^I - \frac{L_Y}{2} \text{ else } X_2^{\beta N} = X_2^\beta$$

$$\text{If } X_3^\beta \geq X_3^I + \frac{L_Z}{2} \text{ then } X_3^{\beta N} = X_3^I + \frac{L_Z}{2} \text{ else } X_3^{\beta N} = X_3^\beta$$

$$\text{If } X_3^\beta \leq X_3^I - \frac{L_Z}{2} \text{ then } X_3^{\beta N} = X_3^I - \frac{L_Z}{2} \text{ else } X_3^{\beta N} = X_3^\beta$$

where the superscript ‘N’ denotes the new value of the position and  $L_x, L_y, L_z$  are the dimensions of the localization box and  $I$  is the centroid of the localization box. Now,

$$\text{If } |X_i^\beta - X_i^\alpha| \leq 10^{-3} \text{ then } R_i = 1 \text{ else}$$

$$R_1 = \frac{(X_1^{\beta N} - X_1^\alpha)}{(X_1^\beta - X_1^\alpha)}$$

$$R_2 = \frac{(X_2^{\beta N} - X_2^\alpha)}{(X_2^\beta - X_2^\alpha)}$$

$$R_3 = \frac{(X_3^{\beta N} - X_3^\alpha)}{(X_3^\beta - X_3^\alpha)}$$

$$\text{If } R_1 \leq R_2 \text{ then } R = R_1, \text{ else } R = R_2. \text{ If } R_3 \leq R \text{ then } R = R_3$$

Then, bond function is given by

$$B^{\alpha\beta} = \frac{R}{L_X L_Y L_z} \quad (4.27)$$

#### 4.6 Atomistic J-integral at Finite Temperature:

From statistical mechanics, the Helmholtz free energy density is given by [25],

$$\Psi = U - T\eta = -\frac{k_B T}{V} \text{Log } Z \quad (4.28)$$

where  $U$  is the internal energy density,  $T$  is the temperature,  $\eta$  is the entropy density,  $V$  is the volume of the ensemble,  $k_B$  is Boltzmann’s constant and  $Z$  is the partition function of the

atoms occupying the region. Note that the general definition of free energy density  $\Psi$  includes the entropy term and therefore is valid for finite temperature applications of the atomistic J-integral. The conventional definition of J-integral under isothermal condition does not consider the entropic contribution to the free energy, and consequently, may lead to significant over-estimation of the J-integral at the atomistic level at elevated temperature. As alluded to in Eq. (4.4), total J-integral at a finite temperature is given by

$$J_T = J_U - J_\eta \quad (4.29)$$

In Eq. (4.29),  $J_U$  is the value of J-integral without considering entropic contribution and is given by Eq. (4.5) and  $J_\eta$  is the entropic contribution. It is evident that at 0 K, the  $T\eta$  in Eq. (4.28) is absent and hence, the equation for  $J_U$  can be used to compute  $J_T$ . However, at higher temperatures,  $T\eta$  term can have significant contribution due to thermal excitation of the atoms leading to a reduction in  $J_T$ . Entropic contribution  $J_\eta$  can be quantified for a defect free crystalline material using the local harmonic (LH) approximation and is given by given by Eq. (4.30) [18].

$$J_\eta = \int_{\partial\Omega} \left\langle \frac{k_B T}{V_\alpha} \log \left( \left( \frac{\hbar}{k_B T} \right)^3 \sqrt{\det D_{LH}} \right) \right\rangle N dA \quad (4.30)$$

In Eq. (27),  $k_B$  is Boltzmann's constant,  $\hbar$  is Planck's constant,  $V_\alpha$  is volume of the atom,  $T$  is the absolute temperature, and  $D_{LH}$  is the dynamical matrix based on the LH approximation of atoms vibrating within a defect-free crystal lattice. The LH approximation is essentially an Einstein model of the vibrational frequencies and has been used extensively in MD-continuum coupling. As shown in Eq. (4.30), computation of the dynamical matrix is necessary to quantify the entropic contribution to J-integral. At elevated temperatures, there is significant random thermal vibration of the atoms about their mean position (not to be confused with the motion of

atoms due to propagating stress waves) and the vibrational modes of the lattice are given by the eigenvalues of the dynamical matrix. The procedure to compute dynamical matrix is discussed in the next section.

#### 4.6.1 Evaluation of dynamical matrix ( $D_{LH}$ )

From statistical mechanics, the dynamical matrix required for quantifying entropic contribution to J-integral is given by [18]),

$$D_{LH} = \frac{1}{2mV} \frac{\partial^2 \Phi}{\partial u_p^2} = \frac{1}{m} \frac{\partial}{\partial u_p} \sum_{\beta \neq P}^N \phi'(r_{\beta P}) \frac{\bar{r}_{\beta P}}{|r_{\beta P}|} \quad (4.31)$$

where,  $\Phi = \frac{1}{2V} \sum_{\alpha} \sum_{\beta \neq 0}^N \phi(r_{\alpha\beta})$  is the potential energy of the crystal per unit volume,  $\bar{r}_{\alpha\beta}$  is the vector representing the average interatomic distance between atoms  $\alpha$  and  $\beta$ , and  $|r_{\alpha\beta}|$  is its magnitude. Because we are dealing with a single atom in the representative volume element (RVE) because of the LH approximation, atom  $\alpha$  is designated as atom P. In Eqn. (4.31),  $u_p$  is the displacement vector representing random thermal motion of atom P about its mean position,  $m$  is the atomic mass,  $\phi(r)$  is the pairwise potential,  $V$  is the volume of the undeformed crystal lattice containing  $N$  atoms,  $\bar{r}_{\beta P}$  is the position vector of atom  $\beta$  measured from the position of the generic atom P, and prime denotes  $\frac{\partial \phi(|r_{\beta P}|)}{\partial |r_{\beta P}|}$ . Using the chain-rule of differentiation, Eq. (4.31) can

be expressed as,

$$D_{LH} = \frac{1}{m} \sum_{\beta \neq P} (\phi''(r_{\beta P}) \frac{\bar{r}_{\beta P}}{r_{\beta P}} \otimes \frac{\bar{r}_{\beta P}}{r_{\beta P}} + \phi'(r_{\beta P}) \frac{1}{r_{\beta P}} [\mathbf{I} - \frac{\bar{r}_{\beta P}}{r_{\beta P}} \otimes \frac{\bar{r}_{\beta P}}{r_{\beta P}}]) \quad (4.32)$$

where,  $\mathbf{I}$  is identity tensor. Using data from MD simulations in Eq. (4.32), the dynamical matrix can be evaluated which can then be used to compute the entropic contribution to J-

integral using Eq. (4.30). For example, consider a pairwise potential given by,

$$\phi(r) = K(|r_{\beta P}| - |r_{\beta P_0}|)^2 \quad (4.33)$$

where,  $K$  is the energy constant and  $r_{\beta P_0}$  is the equilibrium interatomic distance. The position vector of an atom  $\beta$  in rectangular Cartesian coordinates is given by

$$\bar{r}_{\beta} = x_{\beta P} \hat{i} + y_{\beta P} \hat{j} + z_{\beta P} \hat{k} \quad (4.34)$$

And its magnitude is

$$r_{\beta} = \sqrt{x_{\beta P}^2 + y_{\beta P}^2 + z_{\beta P}^2} \quad (4.35)$$

The terms required for evaluation of  $D_{LH}$  can then be written as,

$$\frac{\bar{r}_{\beta}}{r_{\beta}} \otimes \frac{\bar{r}_{\beta}}{r_{\beta}} = \begin{bmatrix} \frac{x_{\beta P}^2}{r_{\beta}^2} & \frac{x_{\beta P} y_{\beta P}}{r_{\beta}^2} & \frac{x_{\beta P} z_{\beta P}}{r_{\beta}^2} \\ \frac{x_{\beta P} y_{\beta P}}{r_{\beta}^2} & \frac{y_{\beta P}^2}{r_{\beta}^2} & \frac{y_{\beta P} z_{\beta P}}{r_{\beta}^2} \\ \frac{x_{\beta P} z_{\beta P}}{r_{\beta}^2} & \frac{y_{\beta P} z_{\beta P}}{r_{\beta}^2} & \frac{z_{\beta P}^2}{r_{\beta}^2} \end{bmatrix} \quad (4.36)$$

$$\mathbf{I} - \frac{\bar{r}_{\beta}}{r_{\beta}} \otimes \frac{\bar{r}_{\beta}}{r_{\beta}} = \begin{bmatrix} 1 - \frac{x_{\beta P}^2}{r_{\beta}^2} & -\frac{x_{\beta P} y_{\beta P}}{r_{\beta}^2} & -\frac{x_{\beta P} z_{\beta P}}{r_{\beta}^2} \\ -\frac{x_{\beta P} y_{\beta P}}{r_{\beta}^2} & 1 - \frac{y_{\beta P}^2}{r_{\beta}^2} & -\frac{y_{\beta P} z_{\beta P}}{r_{\beta}^2} \\ -\frac{x_{\beta P} z_{\beta P}}{r_{\beta}^2} & -\frac{y_{\beta P} z_{\beta P}}{r_{\beta}^2} & 1 - \frac{z_{\beta P}^2}{r_{\beta}^2} \end{bmatrix} \quad (4.37)$$

$$\phi'(r) \frac{1}{r_\beta} \left[ \mathbf{I} - \frac{\bar{r}_\beta}{r_\beta} \otimes \frac{\bar{r}_\beta}{r_\beta} \right] = \frac{2k(r_\beta - r_{\beta P0})}{r_\beta} \begin{bmatrix} 1 - \frac{x_{\beta P}^2}{r_\beta^2} & -\frac{x_{\beta P} y_{\beta P}}{r_\beta^2} & -\frac{x_{\beta P} z_{\beta P}}{r_\beta^2} \\ -\frac{x_{\beta P} y_{\beta P}}{r_\beta^2} & 1 - \frac{y_{\beta P}^2}{r_\beta^2} & -\frac{y_{\beta P} z_{\beta P}}{r_\beta^2} \\ -\frac{x_{\beta P} z_{\beta P}}{r_\beta^2} & -\frac{y_{\beta P} z_{\beta P}}{r_\beta^2} & 1 - \frac{z_{\beta P}^2}{r_\beta^2} \end{bmatrix} \quad (4.38)$$

$$\phi''(r) \frac{\bar{r}_\beta}{r_\beta} \otimes \frac{\bar{r}_\beta}{r_\beta} = 2k \begin{bmatrix} \frac{x_{\beta P}^2}{r_\beta^2} & \frac{x_{\beta P} y_{\beta P}}{r_\beta^2} & \frac{x_{\beta P} z_{\beta P}}{r_\beta^2} \\ \frac{x_{\beta P} y_{\beta P}}{r_\beta^2} & \frac{y_{\beta P}^2}{r_\beta^2} & \frac{y_{\beta P} z_{\beta P}}{r_\beta^2} \\ \frac{x_{\beta P} z_{\beta P}}{r_\beta^2} & \frac{y_{\beta P} z_{\beta P}}{r_\beta^2} & \frac{z_{\beta P}^2}{r_\beta^2} \end{bmatrix} \quad (4.39)$$

Substituting Eq. (4.38) and (4.39) in Eq. (4.32), the final for evaluation of  $D_{LH}$  can then be written as,

$$D_{LH} = \frac{1}{m} \sum_{\beta \neq P} \left( 2k \begin{bmatrix} \frac{x_{\beta P}^2}{r_\beta^2} & \frac{x_{\beta P} y_{\beta P}}{r_\beta^2} & \frac{x_{\beta P} z_{\beta P}}{r_\beta^2} \\ \frac{x_{\beta P} y_{\beta P}}{r_\beta^2} & \frac{y_{\beta P}^2}{r_\beta^2} & \frac{y_{\beta P} z_{\beta P}}{r_\beta^2} \\ \frac{x_{\beta P} z_{\beta P}}{r_\beta^2} & \frac{y_{\beta P} z_{\beta P}}{r_\beta^2} & \frac{z_{\beta P}^2}{r_\beta^2} \end{bmatrix} + \frac{2k(r_\beta - r_{\beta P0})}{r_\beta} \begin{bmatrix} 1 - \frac{x_{\beta P}^2}{r_\beta^2} & -\frac{x_{\beta P} y_{\beta P}}{r_\beta^2} & -\frac{x_{\beta P} z_{\beta P}}{r_\beta^2} \\ -\frac{x_{\beta P} y_{\beta P}}{r_\beta^2} & 1 - \frac{y_{\beta P}^2}{r_\beta^2} & -\frac{y_{\beta P} z_{\beta P}}{r_\beta^2} \\ -\frac{x_{\beta P} z_{\beta P}}{r_\beta^2} & -\frac{y_{\beta P} z_{\beta P}}{r_\beta^2} & 1 - \frac{z_{\beta P}^2}{r_\beta^2} \end{bmatrix} \right) \quad (4.40)$$

Bond order based ReaxFF potential was used to obtain the effective dynamical matrix was attempted. However, the second derivative of the potential energy ( $\phi''$ ) came out negative for a large portion of the deformation domain, resulting in complex determinant of the dynamical matrix. This might be attributed to inaccurate phonon dispersion behavior simulated in graphene due to certain ReaxFF parameters and will be the subject of future investigation. For the present consideration, a harmonic potential of the form given in Eqn. 4.33 was fitted to the bond order based ReaxFF potential using least squares as shown in Figure 4.5. The value of the energy constant,  $K$  obtained from the fit is 219 Kcal/mole at 300 K and was used for the determination

of the  $D_{LH}$  matrix shown in Eqn. 4.41.

$$D_{LH} = \begin{bmatrix} 1.233 & 0 \\ 0 & 1.233 \end{bmatrix} \times 10^4 \text{ Kcal}/(\text{g} \cdot \text{\AA}^2) \quad (4.41)$$

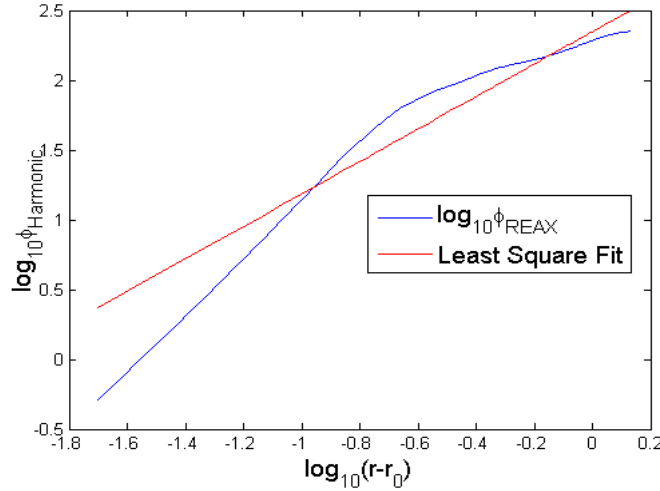


**Figure 4.5:** Evaluation of ReaxFF equivalent energy constant K

The determinant of the 2x2  $D_{LH}$  matrix ( $\det D_{LH}$ ) thus obtained is  $1.52 \times 10^8$ , and was input to equation 4.30 to evaluate the entropic contribution to the atomistic J –integral.

#### 4.7 Numerical Evaluation of Atomistic J-integral:

Numerical integration through Gaussian quadrature was employed to evaluate atomistic J-integral using the equations given in previous sections. The J-integral contour around the crack is divided into seven segments and each segment is further divided into localization boxes, as shown in Figures 4.6 and 4.7. The discrete atomistic values of potentials and displacement gradients obtained from MD simulations were converted into field quantities using the finite element type interpolation functions for a nine node element (given by Eq. (4.42), in terms of element local co-ordinates  $\xi$  and  $\chi$ ) (i.e., set K=9 in Eq. (4.8) and (4.9))

$$\begin{aligned}
N_1 &= \frac{1}{4}(1-\xi)(1-\chi)(\xi\chi) \\
N_2 &= -\frac{1}{4}(1+\xi)(1-\chi)(\xi\chi) \\
N_3 &= \frac{1}{4}(1+\xi)(1+\chi)(\xi\chi) \\
N_4 &= -\frac{1}{4}(1-\xi)(1+\chi)(\xi\chi) \\
N_5 &= -\frac{1}{2}(1-\xi^2)(1-\chi)(\chi) \\
N_6 &= \frac{1}{2}(1+\xi)(1-\chi^2)(\xi) \\
N_7 &= \frac{1}{2}(1-\xi^2)(1+\chi)(\chi) \\
N_8 &= -\frac{1}{2}(1-\xi)(1-\chi^2)(\xi) \\
N_9 &= (1-\xi^2)(1-\chi^2)
\end{aligned} \tag{4.42}$$

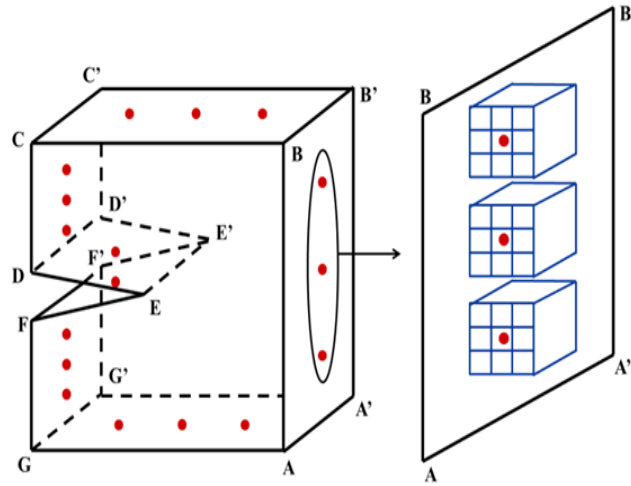


**Figure 4.6:** Gaussian quadrature points along the integration contour depicting localization boxes on one arm

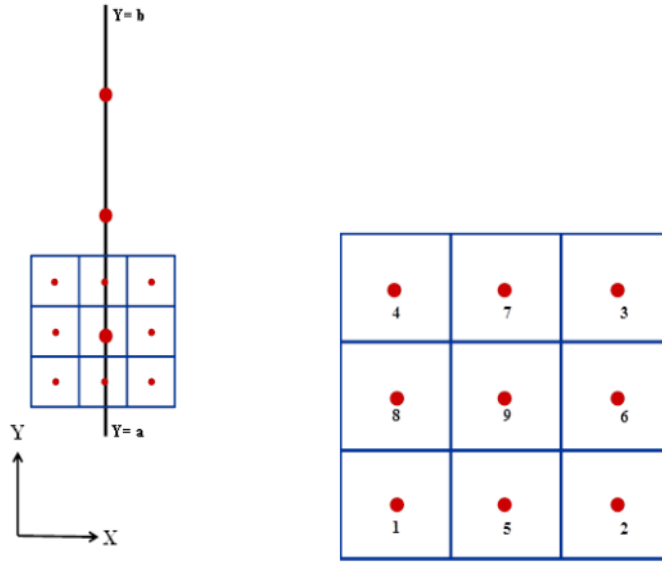


**Figure 4.7:** 9-noded Finite Element framework for computation at the Gauss Points

For example, the energetic part of the J-integral vector for the segment AB is given by,

$$\mathbf{J}_{AB} = h \int_a^b (U \hat{N} - \underline{H}^T \underline{P} \hat{N}) dY \quad (4.43)$$

Referring to Figure 4.8, assuming,  $Y = C_1 \xi + C_2$  and applying boundary conditions,

$a = C_1(-1) + C_2$  and  $b = C_1(1) + C_2$ , leads to  $C_1 = (b-a)/2$  and  $C_2 = (b+a)/2$ . Hence,

$$dY = C_1 d\xi = \left( \frac{b-a}{2} \right) d\xi$$

$$\mathbf{J}_{AB} = h \int_{-1}^1 (U \hat{N} - \underline{H}^T \underline{P} \hat{N}) C_1 d\xi$$

$$\mathbf{J}_{AB} = C_1 h \sum_{k=1}^{N_G} [U(\xi_k) \hat{N} - \underline{H}^T(\xi_k) \underline{P}(\xi_k) \hat{N}] w_k$$

$$\mathbf{J}_{AB} = C_1 h \sum_{k=1}^{N_G} [U(\xi_k) \hat{N} - \underline{H}^T(\xi_k) \underline{P}(\xi_k) \hat{N}] w_k$$

$$\mathbf{J}_{AB} = C_1 h \sum_{k=1}^{N_G} \left[ U(Y_k) \hat{N} - \underline{H}^T(Y_k) \underline{P}(Y_k) \hat{N} \right] w_k$$

where,  $Y_k = C_1 \xi_k + C_2$ ,  $\xi_k$  are the Gaussian quadrature points, and  $w_k$  are the corresponding Gaussian weights, and  $N_G$  is the number of gauss points used in the numerical integration.

J-integral can be calculated using this procedure at all Gaussian quadrature points along each segment, and then summed. Details regarding the graphene sheet used, simulation parameters and simulation results are presented in the next chapter.

**Table 4.1** Sample values of J-integral computed along one path for graphene at 300 K

<b>K (MPa.m<sup>1/2</sup>)</b>	<b>J<sub>I</sub> (J/m<sup>2</sup>)</b>				
	<b>AB</b>	<b>CD</b>	<b>FG</b>	<b>BC</b>	<b>GA</b>
0	0	0	0	0	0
1.809137	1.465201	-0.93596	-0.34054	0	0
2.177237	8.965188	-1.30577	-1.04356	0	0
2.913241	21.26553	-5.0284	-4.53839	0	0

## CHAPTER 5

### MODELLING AND SIMULATION

The modelling and simulation of the nano-graphene sheet is performed by passing through a few modules and steps controlling essential molecular parameters which will be explained below. Periodic boundary condition is maintained in all three directions throughout the procedure.

#### 5.1 Modelling module

A pristine graphene sheet was modelled with height of 20 nm and width of 30 nm with zigzag edge morphology as shown in Figure 5.1. The width was selected to ensure that the tip of the crack introduced in the graphene sheet would not experience spurious interaction effects due to the periodic boundary condition. The pristine graphene sheet consists of 23,616 atoms and was modeled using Virtual Molecular Dynamics (VMD) software [58].

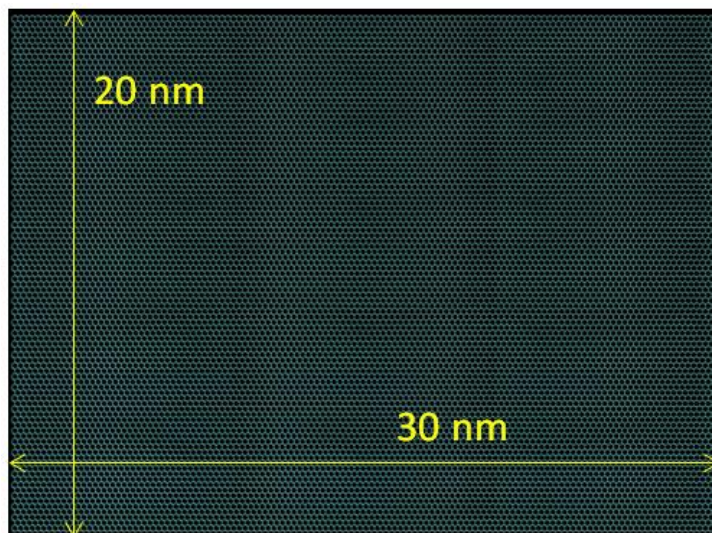


**Figure 5.1:** Modelled graphene sheet in VMD

#### 5.2 Energy-minimization module

The entire graphene system needs to be taken to the most stable equilibrium state

corresponding to its minimum energy configurational state. The energy minimization was done in LAMMPS using its built in Steepest Descent (SD) algorithm. The minimization process was conducted in 0.5 pico-second (5000 steps with timestep size of 0.1 femtosecond). The temperature of the system approached 0 K, and the configuration attained the most stable state feasible in this module.

### **5.3 Thermal equilibration module**

The temperature of the energy-minimized graphene sheet is at 0K. However, the isothermal straining simulation needs to be performed at room temperature. Consequently, the temperature of the graphene system is elevated through a steady stepped-equilibration process in this module for NPT ensemble conserving number of atoms (N), pressure (P) of magnitude 1 bar, and specified temperature (T) for each step of equilibration. NPT equilibration allows stress-free volumetric expansion of the system throughout this module. The said stepped equilibration was conducted by resting (equilibrating all energies) the system at each of the temperatures 10K, 20K, 30K, 60K, 90K, 120K, 150K, 180K, 210K, 240K, 270K for 0.8 picosecond (8000 steps with time-step 0.1 femtosecond) and finally at 300K for 5 picoseconds (50000 steps with time-step 0.1 femtosecond). A stable energy state corresponding to 300K is achieved along with complete absence of any thermally induced out-plane distortions in the graphene sheet after this module. This energy-minimized and thermally equilibrated configuration will now be subjected to the isothermal uniaxial tensile straining at 300K.

### **5.4 Modelling discrete crack for defected sheets**

For modelling the crack of a specific geometry, selected number of lattices was removed from the system producing nano-slits at the center of the sheet as shown in Figure 5.2. During inclusion of vacancy, there are chances of rearrangement of bond forces for which the system

needs to be re-equilibrated in an NPT environment at 300K for 0.3 picosecond.

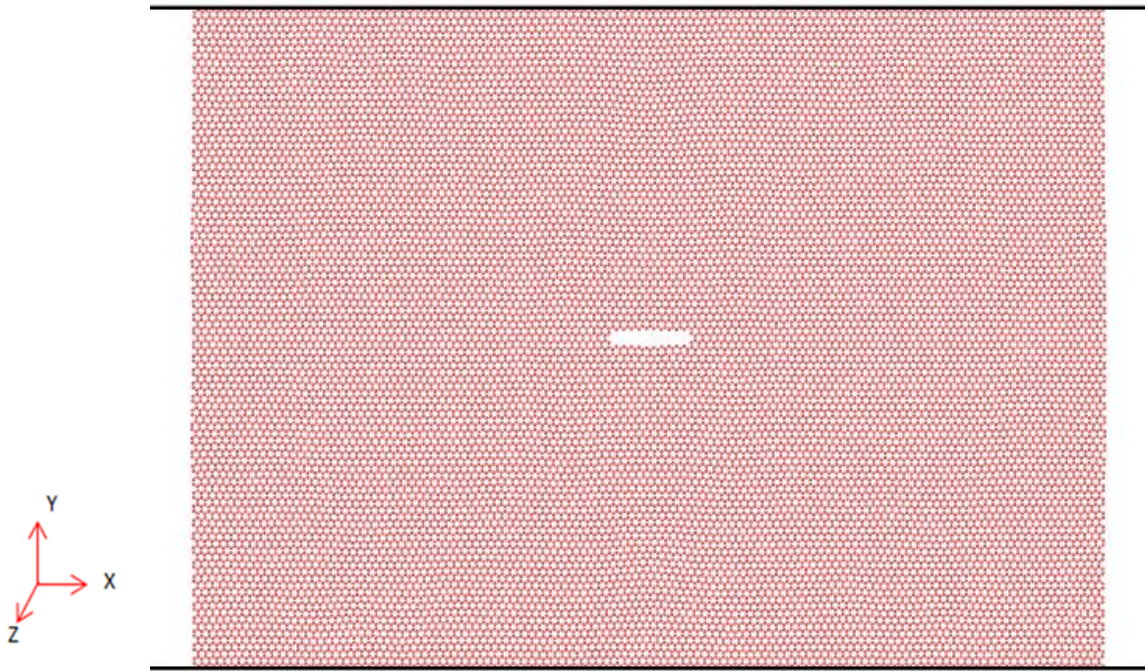


**Figure 5.2:** A 30.59 Å crack is created at the center of the sheet removing 11 hexagonal lattices. X-Y coordinates are shown in the box on left.

### 5.5 Isothermal uniaxial tensile straining module

A steady, step-wise, isothermal uniaxial tensile strain was applied to the system in NVT environment at 300 K temperature at a strain rate of  $1.5 \text{ picosecond}^{-1}$ . Virtual non-periodicity was imposed in boundary condition along X-direction of the system by including small gaps on each side between the simulation box and the vertical edges of the MD model, to safeguard against interactions between adjacent cracks.

During the deformation of the simulation box in the Y-direction, there are risks of eccentric straining due to geometric non-collinearity of top and bottom edges of the atomic system at elevated temperature of 300K due to asymmetrical thermal motion. Consequently, “end-grips” were added into the MD system both along the top and bottom edges (shown by green boxes in Fig. 5.3). For this purpose, the atoms belonging to the so-called end-grip zone

were pre-defined to have zero relative velocity along the Y-direction thereby inducing the required rigid body motion in that zone. The end-grips were 10.76 Å wide and consisted of 1250 atoms on each side (top & bottom) as shown in Figure 5.3. The end grips were located with their centers 96.8Å away from the center of the sheet.

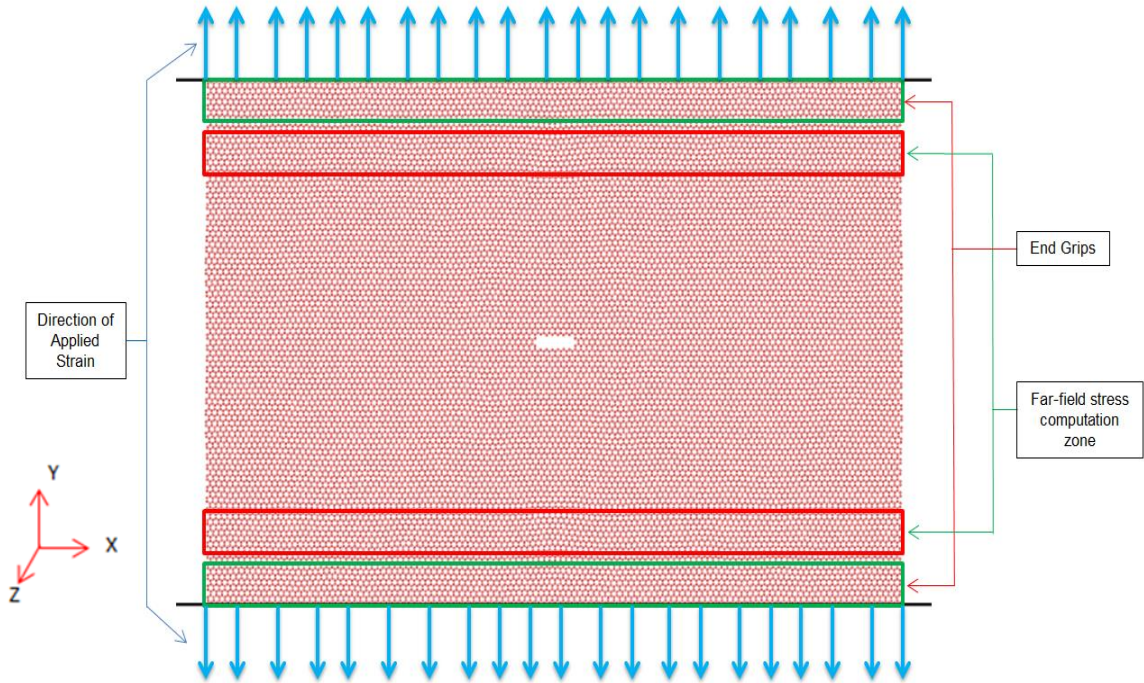


**Figure 5.3:** A typical center-cracked sheet undergoing isothermal tensile straining

For the fracture simulations, strain along the Y-direction was ramped up in piecewise linear steps, with relaxation time in between steps to allow equilibration of the system. For the first ramp step, the simulation box was deformed at a prescribed strain rate of  $1.5 \times 10^{12} \text{ sec}^{-1}$  over 500 time-steps, with each time-step being 0.2 femtosecond. This was followed by relaxation over the next 499 steps (i.e. 99.8 femtoseconds) to allow for equilibration of energy before the next straining step. The process was repeated for subsequent ramp/relaxation steps until fracture of the graphene sheet occurred. In order to ascertain the effect of strain rate on the fracture process in graphene, different strain rates and relaxation times were employed. It was observed through rigorous simulations that the fracture process for graphene was relatively independent of strain

rate if the relaxation ratio, defined to be the ratio of relaxation time to the strain rate, was kept constant.

## 5.6 Post-processing module

Virial stress outputs were obtained from LAMMPS after each simulation. From the definition of virial stress, it comprises of both potential (configurational) and kinetic (thermal) terms. Consequently, the virial stress at the beginning of the deformation was non-zero due to the presence of residual thermal stress in the graphene sheet. Hence, during post-processing, the initial magnitude of virial residual stress was subtracted from the final residual stress to obtain the Cauchy stress at any given point. In this work, continuum interpretation of stresses corresponds to the volumetric average of far-field Cauchy stresses. Therefore, Cauchy stresses were sampled within a zone  $86\text{\AA}$  away from the center of the sheet as shown by red boxes in Fig. 5.3. The geometry of the far-field zone is  $10\text{\AA}$  in height consisting 1196 atoms on each side (top & bottom) as shown in Figure 5.3.

## CHAPTER 6

### RESULTS AND DISCUSSIONS

The results and discussions of all the MD simulations and post-processing are hereby presented in this chapter.

#### 6.1 Isothermal Straining

Various cases were simulated with different initial lengths of the center crack in a single graphene sheet to study the atomistic predictions and compare them with LEFM predictions. At the atomistic scale, crack lengths cannot be selected arbitrarily, and are directly related to the number of atomic lattices removed from the graphene sheet. Table 6.1 shows the length of crack ( $2a$ ) created by the removal of different number of lattices from the center of the sheet.

**TABLE 6.1.** Relationship between lattice removal and crack length

No. of removed lattice 'n'	Length of created crack ' $2a$ ' (Å)
Pristine (n=0)	0
Single-atom defect	2.78
1	4.90
3	9.94
5	15.17
7	20.41
9	25.5
11	30.50

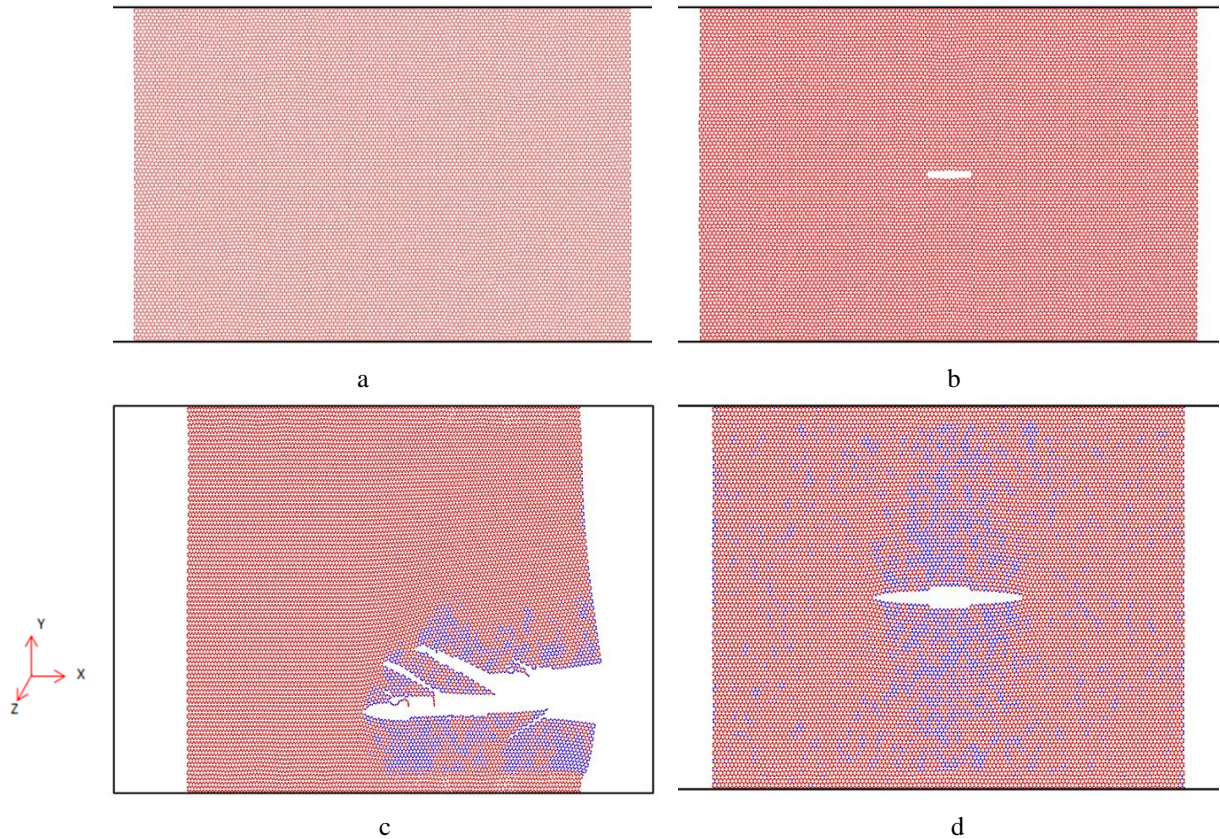


**Figure 6.1:** a)  $n=0$  initial state; b)  $n=11$  initial state; c)  $n=0$  after failure; d)  $n=11$  after failure

Snapshots of the failure simulations for  $n=0$  (initially pristine sheet) and  $n=11$  (large initial crack) cases are shown in Figure 6.1. Figures 6.1(a) and 6.1(b) shows the initial states of both cases while Figures 6.1(c) and 6.1(d) show their states after peak stress is reached and they start failing under mode-I uniaxial tensile strain loading in the Y-direction. As it can be observed, the pristine system with no initial defect exhibits a random damage induced failure at the edge at a strain of 23%. On the other hand, a steady self-similar crack growth was observed for the  $n=11$  case, in conformance with LEFM. Sharp crack propagation leading to brittle failure is observed for this case since it starts failing at about only 6% applied strain. It should be noted that the initial crack length of about  $30\text{\AA}$  is approximately 10% of the total width of the graphene sheet, and therefore the crack tip should not experience spurious edge effects.

For the pristine sheet, the failure stress is found to be 108.24 GPa which is in good

agreement with published the value of 115.05 GPa [59] for graphene. This yields a value of Young’s modulus of 471.3 GPa. This value of Young’s modulus was consistently used throughout all the post processing computations.

The Y-direction stress vs. strain plots for  $n=0$  (pristine) and  $n=11$  cases are shown in Figures 6.2(a) and 6.2(b) respectively (see blue line). For the pristine sheet, a crack tip does not exist, and hence crack-tip bond order could not be shown in the stress strain plot. The green line in Figure 6.2(b) shows the evolution of the Bond Order between two atoms at the crack tip of the sheet with  $n=11$ . The bond order is calculated using equation (3.10). As the bond stretches and  $r_{ij}$  increases with the application of tensile strain, the bond order is steadily reduced and approaches zero when bond failure occurs, as shown in Fig. 6.2(b). It is interesting to note that far-field stress (blue line in Fig 6.2(b)) reaches a peak value just before the bond order at the crack tip reduces to zero, signifying failure initiation. Crack initiation and subsequent failure of the sheet occurs following the peak stress level. The appearance of peak stress where crack-tip bond order reduces to zero, establishes bond order as an effective indicator of failure initiation in a covalently bonded material system undergoing fracture.

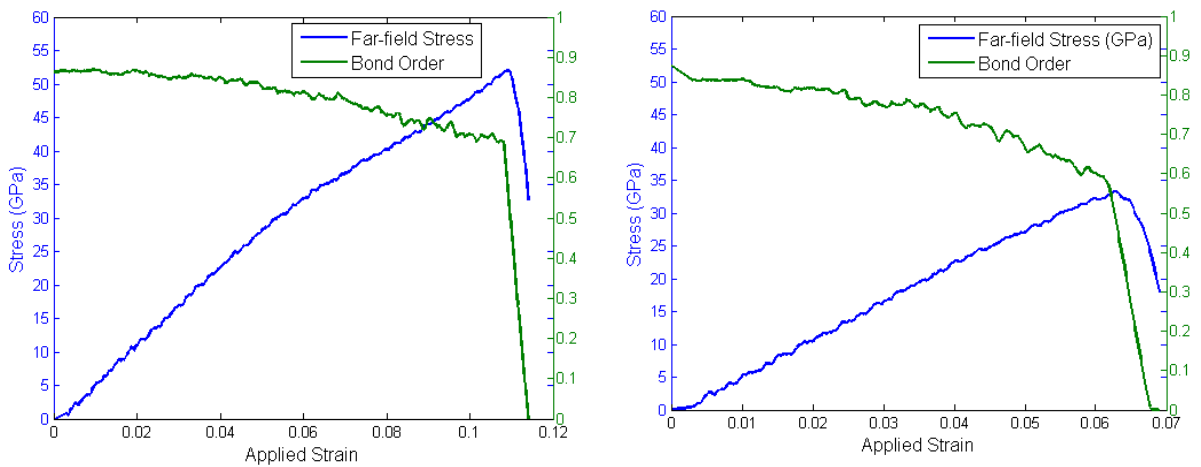


**Figure 6.2:** (a) Far-field stress (blue line) as a function of applied strain for  $n=5$ . (b) Far-field stress (blue line) as a function of applied strain for  $n=11$ . Failure occurs when bond-order goes to zero as shown by the green line.

## 6.2 Length-scale effect of flaw size in nanoscale

The critical far-field stresses were evaluated for graphene sheets with different initial crack lengths using MD simulations. From linear elastic fracture mechanics (LEFM) using modified Griffith's formulation given in equation (4.1), the corresponding far field stress for a given initial crack length was computed for comparison with MD data. These comparisons are plotted in Figure 6.3 for different crack lengths. For LEFM predictions, a Young's modulus  $E$  of 471.3 GPa, surface energy of graphene  $\gamma$  of 5.9 J/m<sup>2</sup> as published in the literature [14], and width of the sheet  $W$  as 30nm were used.

The theoretical value of  $a_{cr}$  was computed to be 1.5Å as stated earlier.

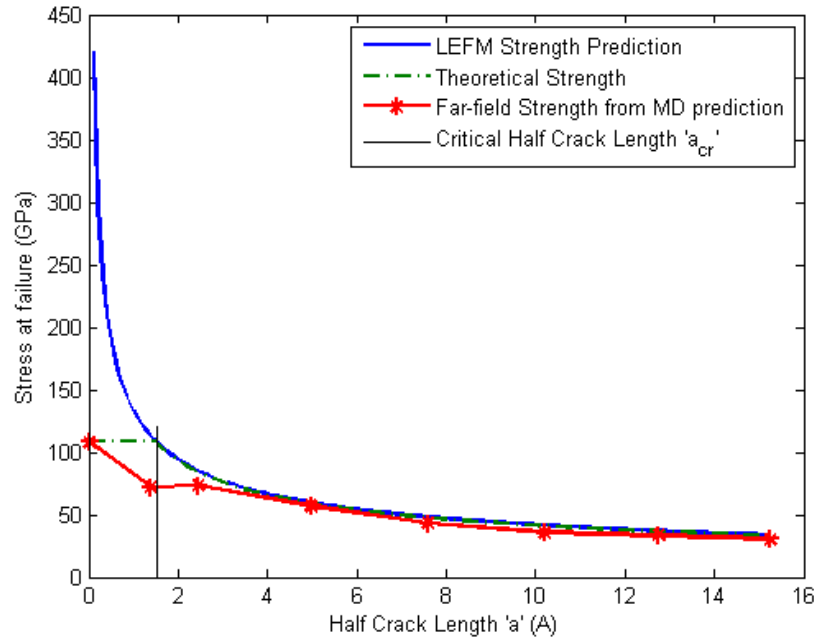


**Figure 6.3:** Stress at failure for each case of initial half-crack lengths

It can be seen that as crack length decreases in Figure 6.3, the critical far-field stress predicted using MD (red curve) closely agrees with LEFM predictions (blue curve) until it reaches a crack length of  $\sim 1.5$  Å. Below the critical crack length of 1.5 Å, a significant difference is observed between MD and LEFM predictions, primarily due to the transition from brittle fracture to strength-based failure in the graphene sheet, thereby rendering LEFM predictions

invalid in that regime. It is notable that the critical crack length of 1.5 Å from MD simulations agrees well with the theoretical prediction of 1.3 Å obtained from eqn. (4.2).

Based on this atomistic study it can be inferred that for materials having lower theoretical strength (like polymers) will have a higher value of  $a_{cr}$ , thereby exhibiting considerable deviation from LEFM predictions over a larger domain of crack lengths.

### 6.3 Comparison with QFM predictions

As shown in Figure 6.4 the far-field stress for a center-cracked graphene sheet obtained using QFM ( $\sigma_{QFM}$ ) is plotted as a function of  $n$ . For  $\rho = 0$  i.e. sharp crack tip, equation (4.3) reduces to the equation for LEFM prediction of far-field stresses with initial crack length of  $l+a/2$ . Hence, the LEFM prediction is also plotted and shown in Figure 6.4 (green curve). For atomistic predictions of quantized far-field stresses, an algorithm was developed to regulate a real-time detection and monitoring of the crack tip during crack growth and stress reduction after the failure is initiated. With every bond breakage and updated crack tip atoms, the far-field atomistic stress was computed in far-field zone and plotted which is shown in Figure 6.4 for comparison with LEFM and QFM predictions.

Figure 6.4 depicts good agreement between QFM, LEFM and atomistic (MD) predictions. The MD data also verifies the QFM premise that at the atomistic scale far-field critical stress is allowed to have certain discrete values corresponding to  $n=1, 2, 3$  etc., with forbidden bands in between, unlike the continuous curve given by LEFM (in green). The likely reason for the consistent deviation of QFM data points from LEFM prediction is due to the radius of the crack tip assumed in QFM.

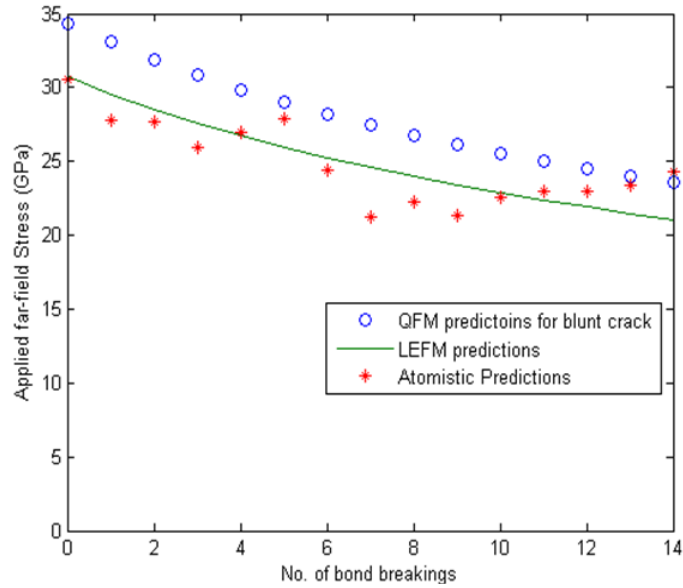


**Figure 6.4:** Accuracy of atomistic predictions in computing quantized far-field

#### 6.4 Non-local effect in nanoscale

As discussed in Section 1.4, non-local effects at the nanoscale due to long-range interatomic forces can also cause significant disagreement of atomistic predictions from that of local continuum-based theories, such as, LEFM. The two aspects that were investigated in this thesis is the existence of finite stress at crack tip and finite traction at crack face at the nanoscale for the nanographene subjected to uniaxial tension.

The stress field ahead of the crack tip along the width of the symmetric nanographene sheet at about 6% strain is plotted (blue curve) in Fig. 10 along with the near-tip LEFM stress field prediction (green curve). The influence of non-locality in nanoscale (MD) is manifested in the existence of finite stress of around 90 GPa at the crack tip in contrast with the infinite stress at the crack tip predicted by LEFM theory. The convergence of the MD stress field to the far-field stress (red-dashed line) applied to the

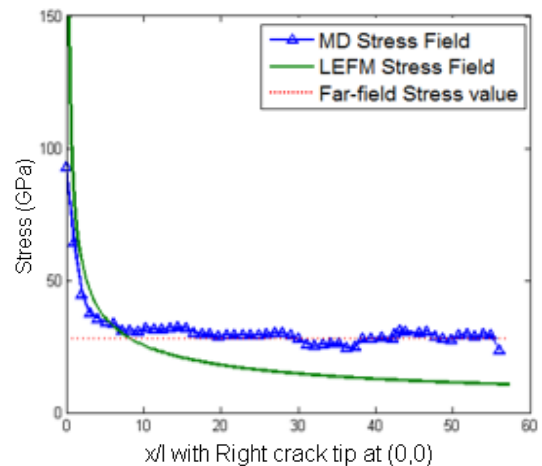


**Figure 6.5:** Existence of finite valued stress at crack tip

graphene system as one moves away from the crack tip, confirms the consistency of the MD result.

Similarly, the average traction on the crack-face from MD is also evaluated to establish the existence of non-local tractions along the supposedly stress-free crack faces. The average traction at the crack face is computed from the temporally and spatially averaged virial stress tensors of the atoms in similar fashion as described in the previous paragraph. Subsequently, the total traction force is computed by multiplying

the average stress with the total area of the crack face to evaluate a strain-based time-history of the total traction force as shown in Fig. 6.6. Figure 6.6 clearly shows the disparity between total traction forces from MD (blue curve) and the traction free LEFM (green line) results at the crack face. Note that the total traction force on the crack face predicted by MD

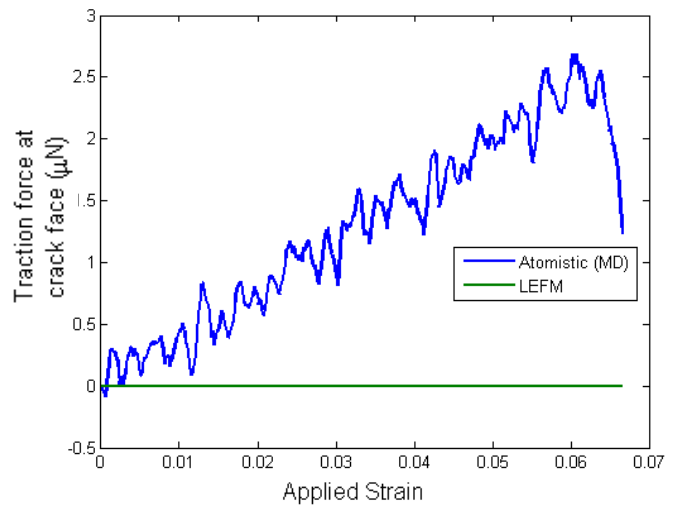


**Figure 6.6:** Evolution of finite traction at the crack face

decreases at crack initiation due to an increase in crack length relative to the cut-off radius for virial stress computation. In the limit, as crack length becomes very large compared with the cut-off radius (i.e., a macro-scale crack), effectively traction-free crack surface is achieved as predicted by LEFM. Appearance of finite traction along the crack face from atomistic predictions again demonstrates the existence of non-locality at the nanoscale in contrast to the traction-free consideration of local continuum-based LEFM theories.

### 6.5 Atomistic J-integral with and without the effect of entropy

This section will focus on evaluation of atomistic J-integral following the procedures described

in sections 4.5 and 4.6. Convergence studies were carried out to ensure the accuracy and robustness of these procedures.

### 6.5.1 Choice of box size

Each of the five arms of the J-integral contour as shown in Fig. 4.6 consists of three Gauss-points (i.e.  $n_g = 3$ ) for computation of the integral along the respective arm through Gaussian quadrature. The computation at each of those Gauss-points can be carried out using Hardy's localization function over the domain of localization-box with the particular Gauss-point as its centroid. The size of the so-called 'localization box' is an important parameter which affects the value of J-integral significantly. Too small a size of the box results in carrying out FEA over very small number of atoms for computation at a Gauss point resulting in inaccurate results. Too large a box size results in high degree of overlap between them due to neighboring Gauss-points along a certain arm of the contour. Thus, a proper choice of this box-size mandates a convergence study of the First Piola-Kirchoff stress as a function of box size, to ensure box-size independence. The values of the First Piola-Kirchoff stress as a function of the l computational box size is shown in Figure 6.7. As can be seen, good convergence in the stress state is achieved beyond a box size of 27 Å. Thus, a box having each side of length 30 Å is selected for all MD stress computations in this thesis.

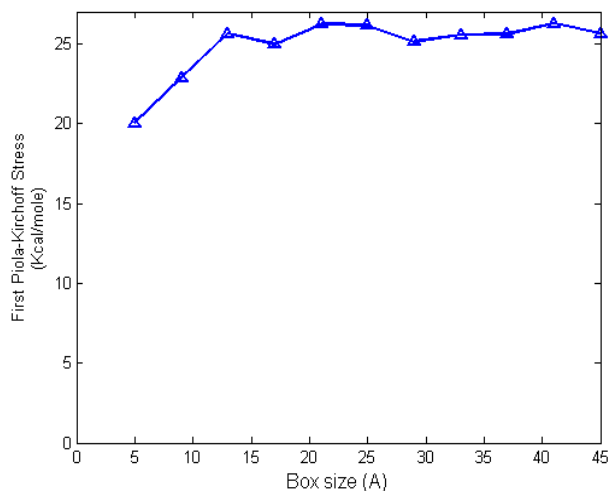


**Figure 6.7 :** Influence of localization box size on computed stress values for graphene

### 6.5.2 Choice of radius of influence cloud

Convergence of Piola-Kirchoff stress is necessary for consistent results of J-integral as stated in the last sub-section. Calculation of Piola-Kirchoff stress needs a stable computation of pair-forces between atoms  $f_{\alpha\beta}$  as shown in equation (4.27). Now, this radius of influence (i.e., cut-off radius) of the ensemble of neighboring atoms  $\beta$  required for computation of total pair-force with respect to an atom  $\alpha$  is a key parameter which affects the consistency of Piola-Kirchoff stress. A convergence study was carried out by varying the length of the radius of influence as shown in Figure 6.8. As can be seen for this figure, a minimum cut-off radius of  $3\text{\AA}$  was sufficient to attain a converged value of the Piola Kirchoff stress, and therefore a cut-off radius of 5 A is chosen for the all MD computations performed in the thesis.

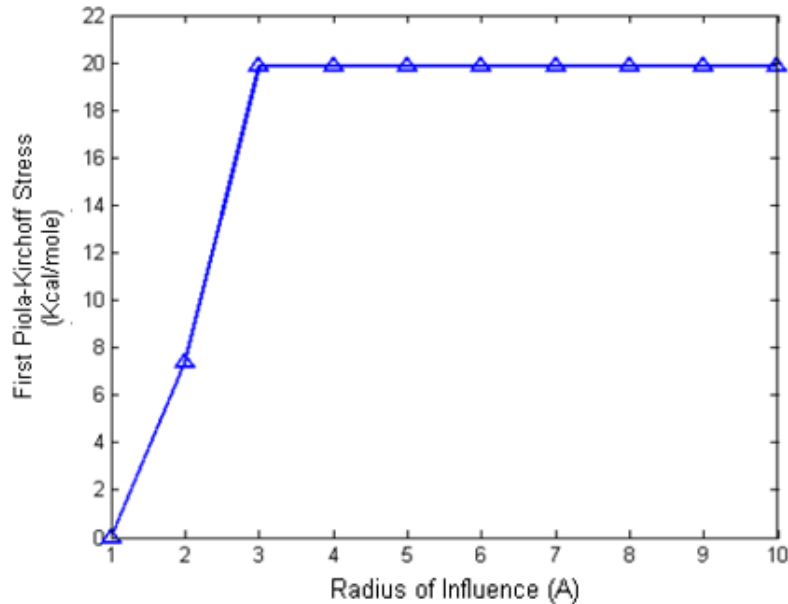


**Figure 6.8** Effect of radius of influence cloud on computed stress values for graphene

### 6.5.3 Validation of path independence of J-integral

In all the results presented in this thesis, J-integral computation was carried out along three concentric contours. Path independence of J is an essential property which needs to be verified to

validate the computed results. The different concentric paths selected are shown in Fig. 6.9.

The result of plotting the energetic component of  $J_I$  vs  $K_I$  obtained along different contours is shown in Fig. 6.10 along with the LEFM prediction. The figure shows considerable path-independence of the J-computation and the LEFM prediction is seen to be passing almost through the average of the three contours until a certain value of  $K_I$ . The deviation of the J-integral curve from LEFM will be discussed in the later sections of this Chapter.

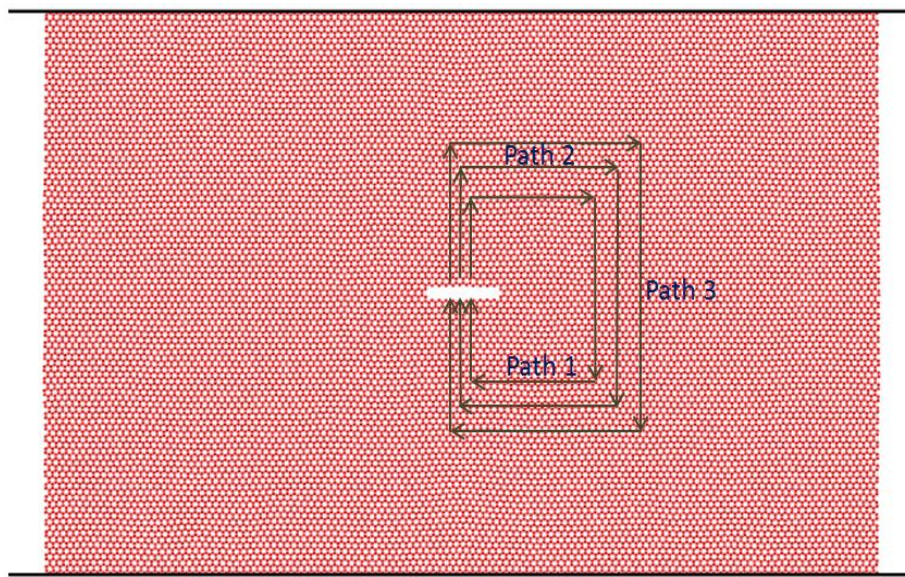


**Figure 6.9** Concentric contours for validation of Path-Independence

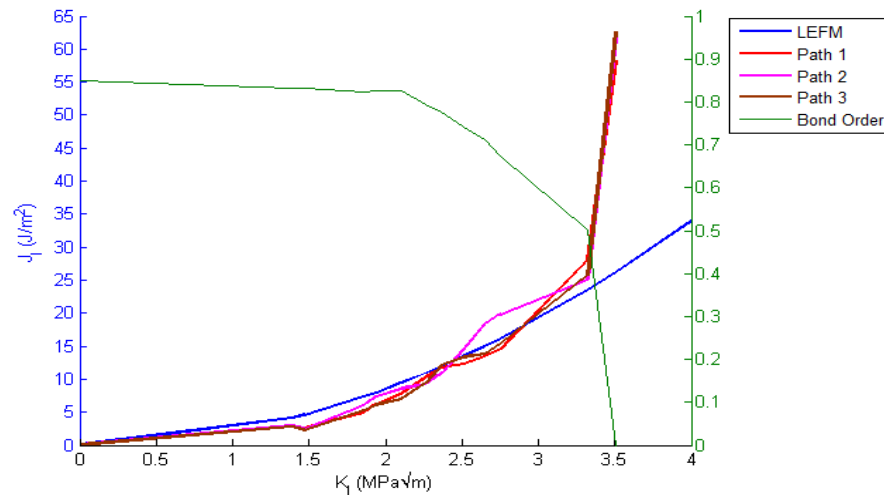


**Figure 6.10** Path Independence of atomistic  $J_U$  (Energetic Component)

### 6.5.4 Computation of $J_2$ component

For a crack to be propagating along x-x direction (i.e., Mode I) implies that the component of  $J$  along the y-y direction is much lower relative to the one along x-x direction. Figure 6.11 shows the time-history of path-independent  $J_2$  along y-y direction, indicating the trivial nature of this component for Mode I crack propagation. It is seen that the plot is oscillating about zero validating the expected trivial nature of this component for Mode I crack propagation. The oscillations of the plot is likely due to thermal vibration of atoms at 300 K.

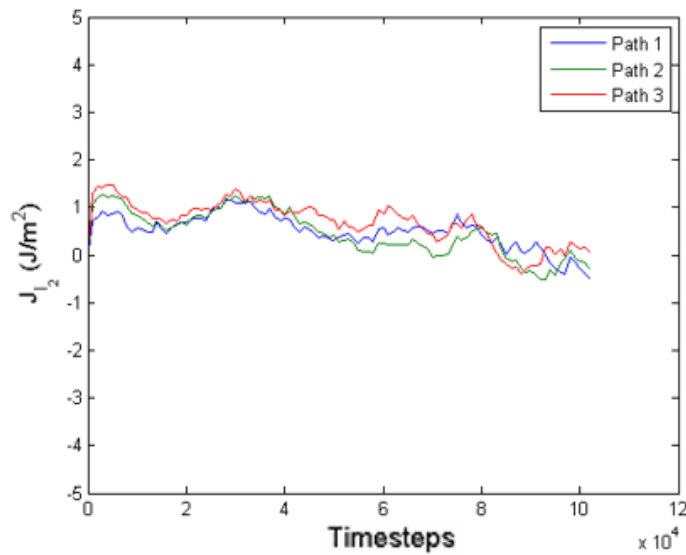


**Figure 6.11** Non-existence of the path independent y-y component of atomistic  $J_U$

### 6.5.5 Path Independence of the entropic component

The dynamical matrix  $D_{LH}$  matrix was evaluated, based on which the entropic contribution of the J-integral was computed at different configurational states. The result obtained plotting the entropic component  $J_\eta$  at various states of  $K_I$  along different contours is shown in Fig. 6.12 along with Bond Order. The figure clearly shows good path-independence of the entropic J-computation.

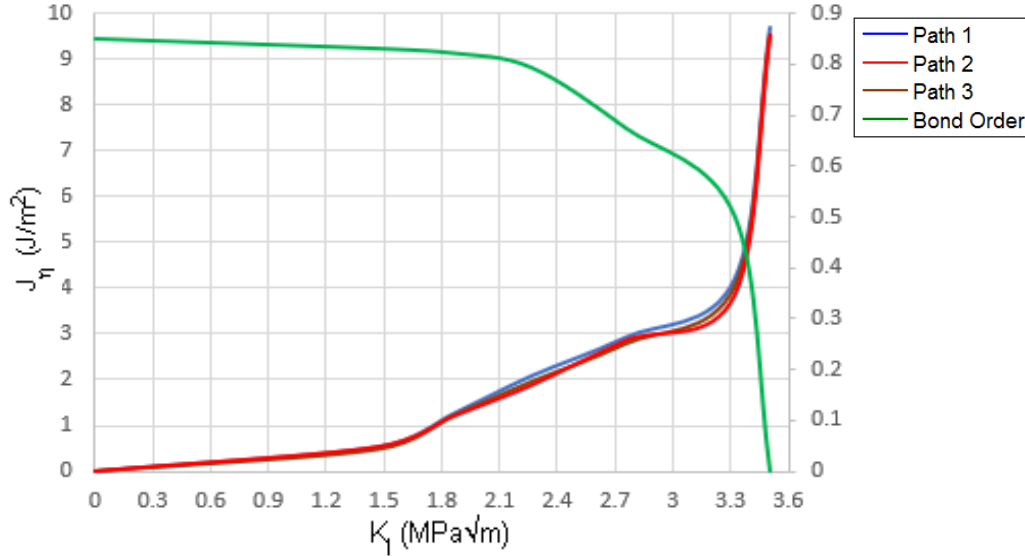


**Figure 6.12** Path Independence of atomistic  $J_{\eta}$  (Entropic Component)

### 6.5.6 Computed $J_I$ vs $K_I$ with and without considering entropic effects

Based on the results discussed in Section 3.1, it was established that for a computation box size of 30 Å, the J-integral computations are independent of localization box size. Figure 6.13 shows the comparison of atomistic J-integral computed at 300 K for a zig-zag configuration compared with LEFM predictions for a localization box size of 30 Å (averaged over three concentric contours). In Fig. 6.13 (a),  $J_U$  (in blue) is the portion of the atomistic J-integral which includes only internal energy contribution, (that is, without including entropic contribution). The ordinate on the right-hand side of the plot depicts the variation in bond order between the atoms just ahead of the crack tip. It can be observed that as the sheet is stretched in tension, the atomic bond gets stretched, and accordingly the bond order decreases as a function of loading ( $K_I$ ). When the bond order goes to zero the bond is effectively broken, providing a critical value of  $J$  ( $J_{Ic}$ ) at crack initiation. As can be observed from Fig 6.13, there is good agreement between LEFM (in red) and the energetic component of J-integral ( $J_U$ ) until the bond order (in green) at the crack tip reduces to zero, indicating crack initiation. As the crack initiates and starts to propagate the atomistic  $J_U$  increases abruptly to capture local intensification of the energy release

rate, which conventional LEFM is unable to account for due to lack of an embedded failure criterion. Similarly, in Fig. 6.13 (b),  $J_T$  (in blue) is the total computed atomistic J-integral including both energetic and entropic contributions, calculated using the local harmonic approximation, as discussed in Sections 2.3 and 2.4. However, using the classical definition of J (i.e.,  $J_T=J_U$ ) does not account for the entropic contribution that becomes significant at higher temperatures, as underscored by the difference between the total J-integral ( $J_T$ ) and the energetic J-integral ( $J_U$ ) computed at 300K as shown in Figures 6.13(a) and (b). With increasing temperature, the entropic contribution becomes ever more significant leading to the reduction of predicted value of total J ( $J_T$ ) from LEFM predictions, as mandated by Eqn. (9). Interestingly, as shown in Figure 6.13, the  $J_T$  curve, analogous to the  $J_U$  curve, increases abruptly marking a temporally local release of energy at the instant of crack initiation as the bond order goes to zero, and this total fracture toughness value at 300 K ( $J_{TC} = \sim 22 \text{ J/m}^2$ ), which is 15% less than that of the energetic component ( $J_{UC} = \sim 26 \text{ J/m}^2$ ) agrees reasonably with its measured value published in the literature ( $J_{Ic} = \sim 16 \text{ J/m}^2$  [9]) for graphene at 300 K. The undulations in the bond order value at 300 K are possibly because of thermal excitation of atoms at elevated temperature. The results indicate that the reduction of bond order to zero corresponds fairly well with when the value of computed J-integral abruptly deviates from LEFM predictions and crack initiation occurs. It also underscores the fact that the entropic contribution to total J at 300 K is approximately 15% and is likely to increase at higher temperatures. This rapid change of slope of  $J_I$  vs.  $K_I$  could be considered as the point of crack initiation and could directly be related to the fracture toughness of the material system in a predictive sense.

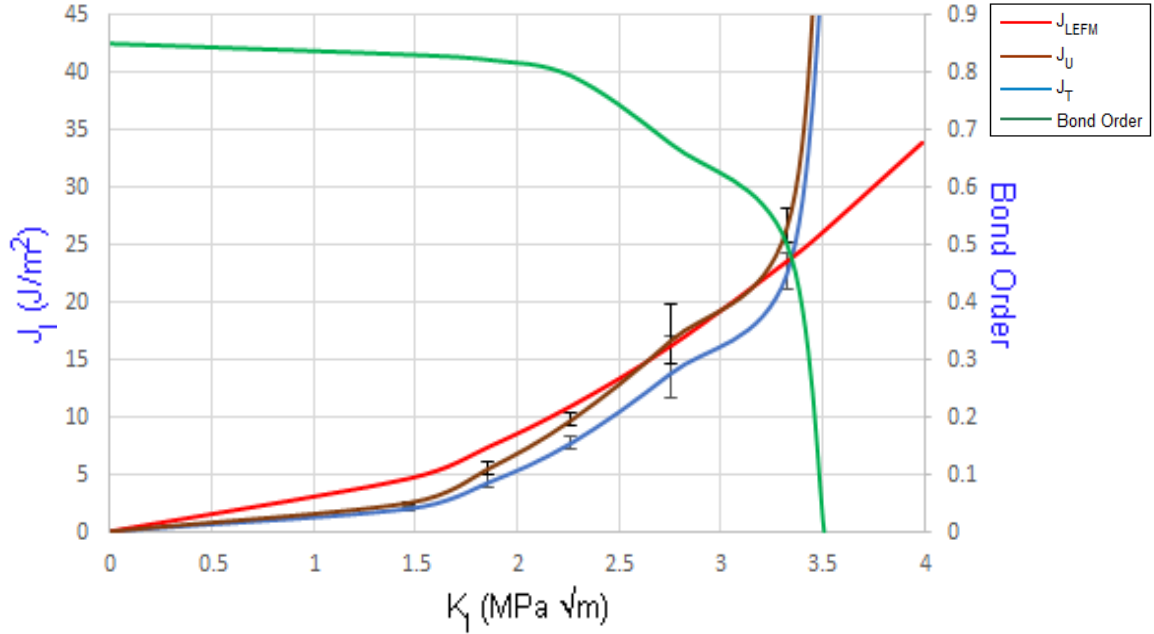


**Figure 6.13** Atomistic J-integral computations in graphene with zig-zag morphology as a function of  $K_I$  for purely energetic contribution and total (with energetic and entropic) contributions at 300K shown along with change in Bond Order at the crack tip

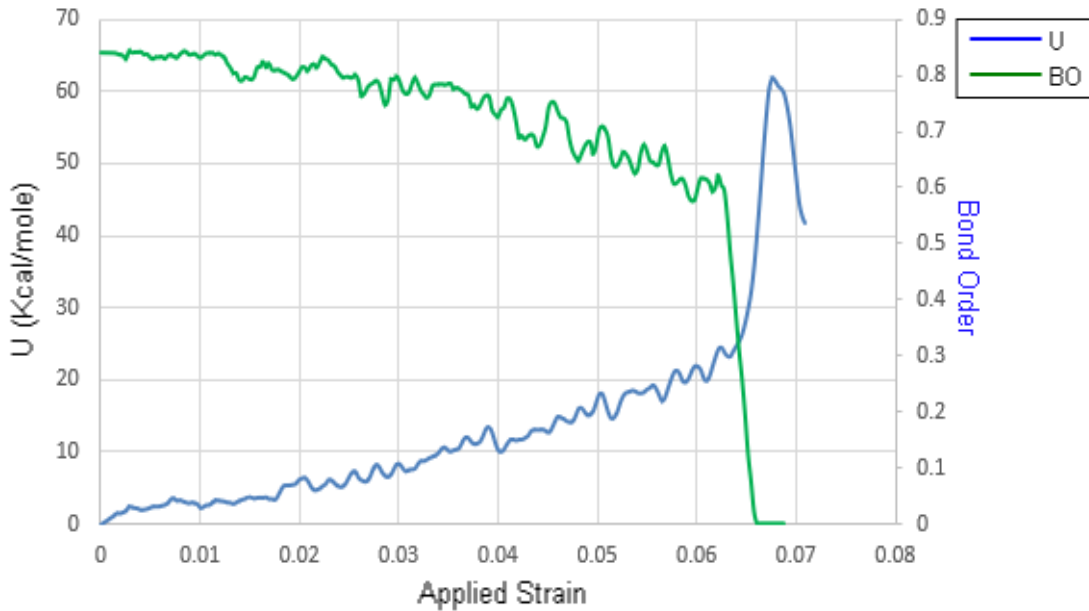
### 6.5.7 Tracking internal energy density (U), First Piola-Kirchoff Stress (P) and Displacement Gradient Tensor (H) at crack initiation and during crack growth

The x-component of the J-integral i.e.  $J_1$  can be evaluated from equation 4.5 and can be written as

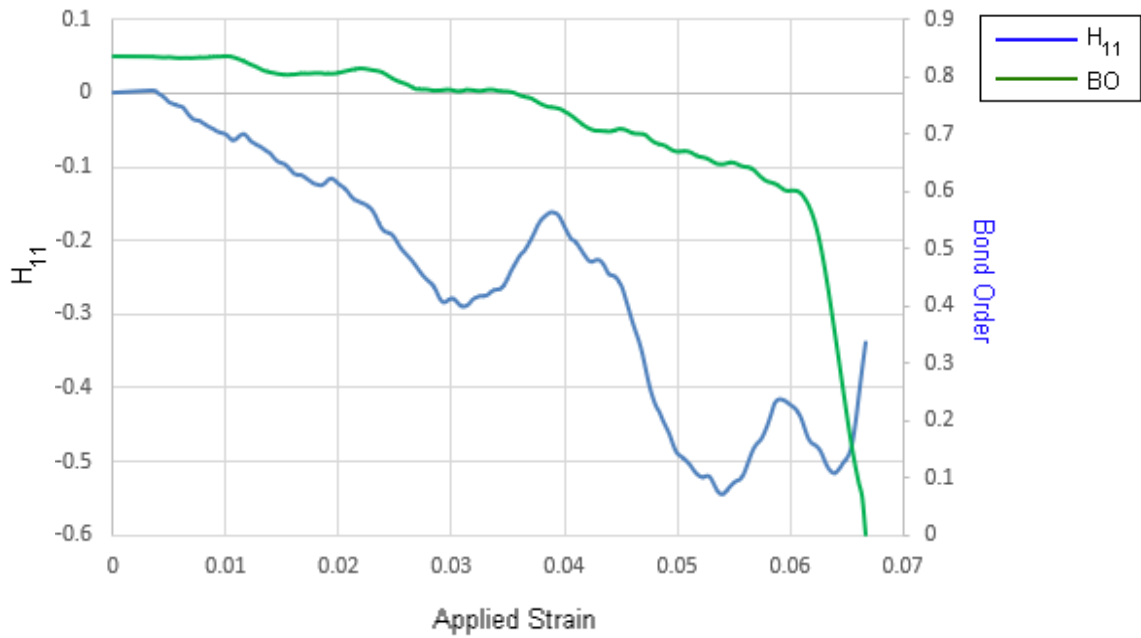
$$J_1 = \int_{\partial\Omega} [UN_1 - \mathbf{H}_{11}\mathbf{P}_{11}N_1 - \mathbf{H}_{21}\mathbf{P}_{21}N_1 - \mathbf{H}_{11}\mathbf{P}_{12}N_2 - \mathbf{H}_{21}\mathbf{P}_{22}N_2] dA \quad (6.1)$$

For Mode I loading considered in this case study, the magnitudes of  $H_{12}$ ,  $H_{21}$ ,  $P_{12}$  and  $P_{21}$  are extremely small and insignificant relative to those of  $H_{11}$ ,  $H_{22}$ ,  $P_{11}$  and  $P_{22}$  resulting in the dependence of  $J_1$  only on these components of both the displacement gradient tensor and the first Piola-Kirchoff stress tensor. Therefore, internal energy density (U), components of first Piola-Kirchoff stress ( $P_{11}$ ,  $P_{22}$ ) and displacement gradient ( $H_{11}$ ,  $H_{22}$ ) tensors were obtained performing Gaussian quadrature over computations at each Gauss point along the J-contour path and summed, as defined in Eqn. 6.1, for various strain states until the initiation of the crack at the

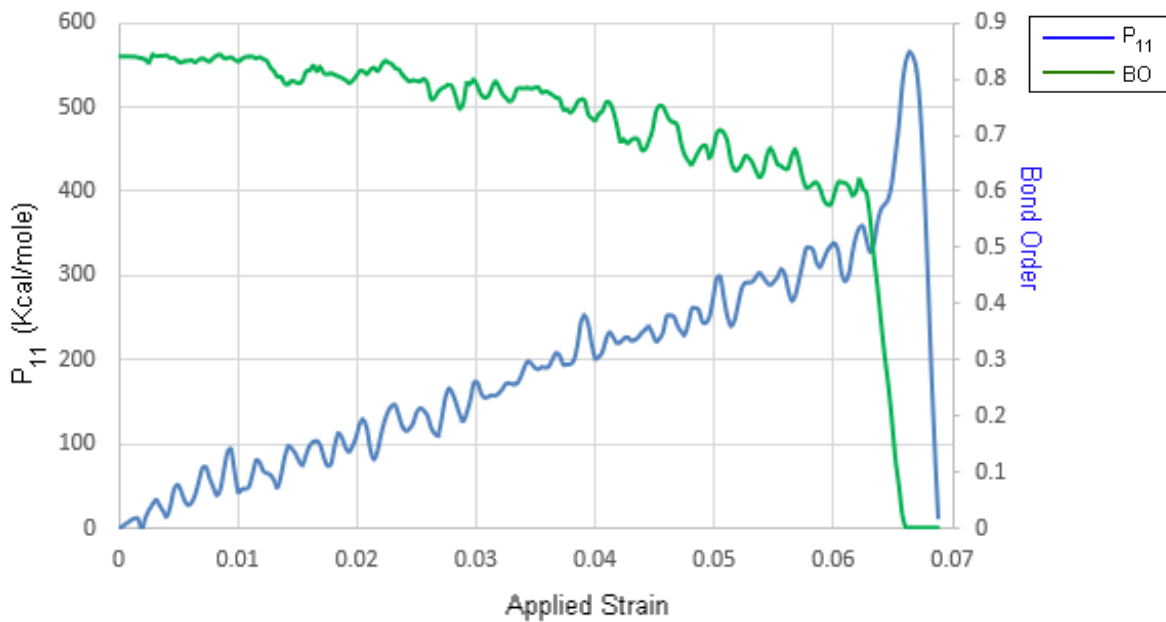
center of the sheet as well as during crack growth. As seen from Figure 6.14 (a), as the crack starts initiating as indicated by the crack-tip bond-order going to zero, the internal energy density increases abruptly as the crack initiates, followed by a reduction in internal energy density as the crack begins to grow. . Similarly, in Fig. 6.14 (b) the  $H_{11}$  component of the deformation gradient decreases monotonically until the crack starts initiating after which it decreases to zero. Finally, in Fig. 6.14 (c) the  $P_{11}$  component of the first Piola-Kirchoff stress attains its peak value as the crack starts initiating after which it rapidly reduces to zero. Thus, internal energy being the sole contributor, after the crack starts initiating, the resulting energetic component of J-integral follows the trend of the internal energy vs strain plot from that point.



(a)



(b)



(c)

**Figure 6.14** Computed (a) internal energy density ( $U$ ), components of (b) displacement gradient tensor ( $H_{11}$ ), (c) first Piola-Kirchoff stress tensor ( $P_{11}$ ) with incremental strain shown along with varying Bond Order at crack tip for center crack length of  $30.95 \text{ \AA}$

## CHAPTER 7

### CONCLUSION AND FUTURE WORK

Ability of atomistic predictions in quantifying fracture mechanisms was established in this thesis for crystalline material like graphene. The failure of LEFM in predicting fracture behavior below certain critical length-scale was underscored. Due to its inherent ability to model bond breakage, ReaxFF potential was used to successfully model crack propagation in a graphene sheet. Atomistic predictions were observed to deviate from LEFM predictions for cases of sheets having their half-crack length below the  $a_{cr}$ . The atomistic prediction of theoretical strength for pristine case was validated from published data and they are seen to be close enough to be considered reliable. Following theoretical predictions, MD predictions were seen to converge and show considerable agreement with LEFM predictions for the cases of graphene sheets having their initial half-crack lengths greater than  $a_{cr}$  which again validates the trend of atomistic predictions. A stress jump was observed for atomistic predictions between pristine (no defect) and single-atom defect case, which was supposed to be flat as per theoretical expectations. But that jump is attributed to appearance of a finite vacancy with even a single atom defect with respect to the pristine case. This effect will be clearer for polymers or other amorphous materials having low strengths and high value of  $a_{cr}$  allowing higher resolution of crack lengths below the critical value. Consistency of atomistic prediction with that of continuum were checked and confirmed for certain cases through fracture strength, QFM etc. The

post-processed MD simulated system were also employed in predicting post-crack-initiation behavior of the material and compared with predictions based on QFM approach. A good agreement was achieved between the atomistic and LEFM predictions for a case of half-crack length higher than  $a_{cr}$  which opens a lot of scope of application of the atomistic predictions to post-crack-initiation timesteps to those cases having half crack lengths below  $a_{cr}$  where LEFM loses its validity. Effect of non-locality was also recognized, investigated and reported through existence of finite stress at crack tip and also evolution of finite traction at crack face in contrast to LEFM considerations. A methodology for using atomistic J was revisited, including energetic and entropic effects, and discussed in detail. The atomistic J-integral values were found to be in good agreement with the values available in the literature.

Future work would include determination of how nanoparticles can be employed as matrix reinforcement of optimized size to maintain a flaw size less than the critical value such that debond cracks along nanoparticle-polymer interface will remain below a critical length scale thereby enhancing toughness. The fracture properties prediction methodology discussed in this thesis could be extended to amorphous polymer systems with appropriate potential functions. However, the use of Local Harmonic approximation employed in the determination of the dynamical matrix for graphene will no longer be applicable for an amorphous polymer, and a new technique will need to be developed to obtain the entropic component of J. The change in values of J-integral with crack propagation could be used to develop resistance curves (R-curve) for polymers with nanoscale reinforcements. The data obtained from these nanoscale studies can be used in multiscale analysis of advanced materials. Appropriate computational tools such as molecular dynamics at nanoscale, generalized method of cells at micro-scale and finite element analysis at macro-scale should be used to effectively transfer information from one length scale

to the other in order to reduce the total computation time. One such hierarchical multiscale modeling scheme is illustrated in Figure 7. Here, atomistic J-integral data from nanoscale MD simulations can be input into microscale analysis using techniques such as generalized method of cells (GMC) including the influence of nanoparticle on the fracture toughness of the polymer matrix. The microscale model is, in turn, called by a macroscale finite element analysis model (FEA) at each element integration point, and failure of fiber and/or matrix is determined at that point. If there is failure at the microscale, then load redistribution takes place at the macroscale through element stiffness reduction. The process is repeated iteratively. In this manner, the hierarchical multiscale technique could be employed to predict progressive failure in nanoparticle reinforced composite material at the structural level.

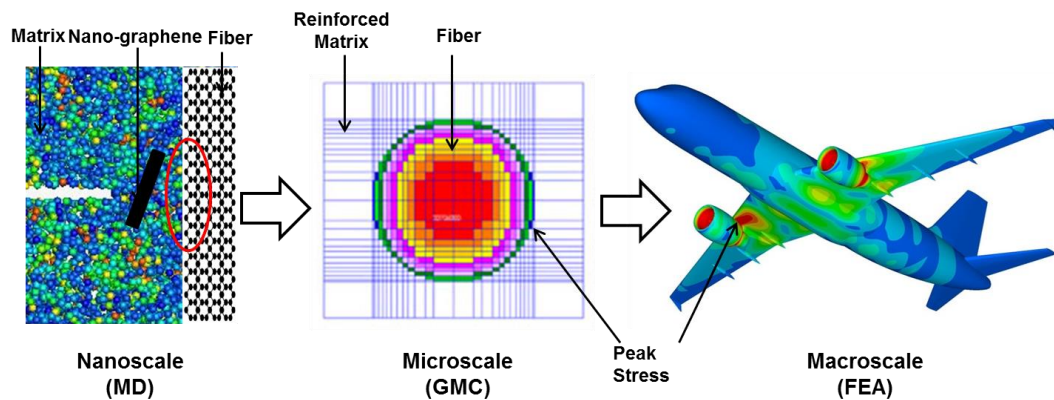


**Figure 7** Schematic of a hierarchical multiscale model for analysis of structures

## REFERENCES

- [1] S. Roy, H. Lu, K. Vengadassalam, and F. Hussain. "Compressive Strength Enhancement of Pultruded Thermoplastic Composites Using Nanoclay Reinforcement." In 45th AIAA/ASME/ASCE/AHS/ASC Structures, Structural Dynamics & Materials Conference, p. 1778. 2004.
- [2] Y. Zhou, F. Pervin, S. Jeelani, and P. K. Mallick. "Improvement in mechanical properties of carbon fabric–epoxy composite using carbon nanofibers." *Journal of materials processing technology* 198, no. 1-3 (2008): 445-453.
- [3] F. H. Gojny, M. H. G. Wichmann, U. Köpke, B. Fiedler, and K. Schulte. "Carbon nanotube-reinforced epoxy-composites: enhanced stiffness and fracture toughness at low nanotube content." *Composites science and technology* 64, no. 15 (2004): 2363-2371.
- [4] W. Liu, S. V. Hoa, and M. Pugh. "Fracture toughness and water uptake of high-performance epoxy/nanoclay nanocomposites." *Composites Science and Technology* 65, no. 15-16 (2005): 2364-2373.
- [5] S. S. Wicks, and B. L. Wardle. "Interlaminar fracture toughness of laminated woven composites reinforced with aligned nanoscale fibers: mechanisms at the macro, micro, and nano scales." In 54th AIAA/ASME/ASCE/AHS/ASC Structures, Structural Dynamics, and Materials Conference, p. 1612. (2013).
- [6] A. Kumar, S. Li, S. Roy, J. A. King and G. M. Odegard, Fracture properties of nanographene reinforced EPON 862 thermoset polymer system. *Composites Science and Technology*, 114, (2015) 87-93.
- [7] A. Kumar, and S. Roy. Characterization of mixed mode fracture properties of nanographene reinforced epoxy and Mode I delamination of its carbon fiber composite. *Composites Part B: Engineering* 134 (2018): 98-105.
- [8] M. A. Rafiee, J. Rafiee, I. Srivastava, Z. Wang, H. Song, Z. Yu, and N. Koratkar. "Fracture and fatigue in graphene nanocomposites." *small* 6, no. 2 (2010): 179-183.
- [9] P. Zhang, L. Ma, F. Fan, Z. Zeng, C. Peng, P. E. Loya, Fracture toughness of graphene, *Nature communications* 5 (2014): 3782.
- [10] N. M. Pugno, R. S. Ruoff, Quantized fracture mechanics. *Philosophical Magazine* 84, no. 27 (2004): 2829-2845.

- [11] H. Gao, B. Ji, I. L. Jäger, E. Arzt, P. Fratzl. Materials become insensitive to flaws at nanoscale: lessons from nature, *Proceedings of the national Academy of Sciences* 100, no. 10 (2003): 5597-5600.
- [12] M. A. N. Dewapriya, R. K. N. D. Rajapakse, A. S. Phani. Atomistic and continuum modelling of temperature-dependent fracture of graphene, *International Journal of Fracture* 187, no. 2 (2014): 199-212.
- [13] L. Wang, Z. Zhang, X. Han, In situ experimental mechanics of nanomaterials at the atomic scale, *NPG Asia Materials* 5, no. 2 (2013): e40.
- [14] R. Khare, S. L. Mielke, J. T. Paci, S. Zhang, R. Ballarini, G. C. Schatz et al., “Coupled quantum mechanical/molecular mechanical modeling of the fracture of defective carbon nanotubes and graphene sheets”, *Physical Review B* 75, no. 7 (2007): 075412.
- [15] M. P. Allen, D. J. Tildesley, “Molecular Simulation of Liquids. Clarendon”, Oxford. 1987.
- [16] S-H Cheng, C. T. Sun. Size-dependent fracture toughness of nanoscale structures: crack-tip stress approach in molecular dynamics, *Journal of Nanomechanics and Micromechanics* 4, no. 4 (2013): A4014001.
- [17] G. M. Odegard, T. C. Clancy, T. S. Gates., Modeling of the mechanical properties of nanoparticle/polymer composites, *Polymer* 46, no. 2 (2005): 553-562.
- [18] R. E. Jones, J. A. Zimmerman, J. Oswald, T. Belytschko, An atomistic J-integral at finite temperature based on Hardy estimates of continuum fields, *Journal of Physics: Condensed Matter* 23, no. 1 (2010): 015002.
- [19] S. Roy, A. Nair., Concurrent multi-scale modeling of nano-particle reinforced polymers using statistical coupling of MD and GIMPM, In 52nd AIAA/ASME/ASCE/AHS/ASC Structures, Structural Dynamics and Materials Conference 19th AIAA/ASME/AHS Adaptive Structures Conference 13t, p. 1922. 2011.
- [20] S. Roy, A. Akepati, Multi-scale Modeling of Failure in Nano-Particle Reinforced Polymers Using the Atomistic J-Integral, In 55th AIAA/ASMe/ASCE/AHS/SC Structures, Structural Dynamics, and Materials Conference, (2014) p. 0106.
- [21] P. Upadhyaya, S. Singh, S. Roy., A mechanism-based multi-scale model for predicting thermo-oxidative degradation in high temperature polymer matrix composites, *Composites Science and Technology* 71, no. 10 (2011): 1309-1315.
- [22] S. L. Mielke, T. Belytschko, G. C. Schatz., Nanoscale fracture mechanics., *Annu. Rev. Phys. Chem.* 58 (2007): 185-209.
- [23] F. F. Abraham, D. Brodbeck, W. E. Rudge, X. Xu, “A molecular dynamics investigation of rapid fracture mechanics”, *Journal of the Mechanics and Physics of Solids*, (1997);45(9):1595-619.

- [24] H. Gao H, Y. Huang, F. F. Abraham, “Continuum and atomistic studies of intersonic crack propagation”, *Journal of the Mechanics and Physics of Solids*. (2001);49(9):2113-32.
- [25] J. H. Weiner, “Statistical Mechanics in Elasticity”, *John Wiley & Sons* (1983)
- [26] A. C. Eringen, D. G. B. Edelen, “On nonlocal elasticity”, *International Journal of Engineering Science* 10, no. 3 (1972): 233-248.
- [27] G. Allegri, F. L. Scarpa, “On the asymptotic crack-tip stress fields in nonlocal orthotropic elasticity”, *International Journal of Solids and Structures* 51, no. 2 (2014): 504-515
- [28] J. R. Rice, A path independent integral and the approximate analysis of strain concentration by notches and cracks. *Journal of Applied Mechanics*, 35(2), (1968), 379–386
- [29] J. Begley and J. Landes, J-integral as fracture criterion. *American Society for Testing of Materials*, (1972), 514:1-20.
- [30] S. Mindess, F. V. Lawrence, and C. E. Kesler, The J-integral as a fracture criterion for fiber reinforced concrete. *Cement and Concrete Research*, 7(6), (1977), 731-742.
- [31] R. E. Jones, and J. A. Zimmerman, The construction and application of an atomistic J-integral via Hardy estimates of continuum fields. *Journal of the Mechanics and Physics of Solids*, 58(9), (2010), 1318–1337.
- [32] J. A. Zimmerman, and R. E. Jones, The application of an atomistic J-integral to a ductile crack. *Journal of Physics. Condensed Matter*, 25, (2013), 155402
- [33] J. D. Eshelby, The elastic energy-momentum tensor. *Journal of Elasticity*, 5, (1975), 321–335.
- [34] H. Inoue, Y. Akahoshi, and S. Harada, A fracture parameter for Molecular Dynamics method. *International Journal of Fracture*, 66(4), (1994), R77–R81
- [35] Z. H. Jin, C. T. Sun, On J-integral and potential energy variation. *International journal of fracture*, 126(1), (2004) L19-L24.)
- [36] R. J. Hardy, Formulas for determining local properties in molecular dynamics simulations: Shock waves. *The Journal of Chemical Physics*, 76(1), (1982), 622–628.
- [37] K. Nakatani, N. Akihiro, S. Yoshihiko, H. Kitagawa, Molecular dynamics study on mechanical properties and fracture in amorphous metal, *AIAA*, (2000), 38(4).
- [38] Y. G. Xu, K. Behdian, and Z. Fawaz, Molecular dynamics calculation of the J-integral fracture criterion for nano-sized crystals. *International Journal of Fracture*, 130(2), (2004), 571–583.

- [39] A. Latapie, and D. Farkas, Molecular dynamics investigation of the fracture behavior of nanocrystalline  $\alpha$ -Fe. *Physical Review B*, 69(13), (2004), 134110
- [40] Large Scale Atomic/Molecular Massively Parallel Simulator (LAMMPS) available at: <http://lammps.sandia.gov>. (2013)
- [41] Zepeda-Ruiz, Stukowski, Oettel, and Bulatov: Probing the limits of metal plasticity with molecular dynamics simulations, *Nature* 550, 492–495
- [42] L. Verlet, Computer "experiments" on classical fluids. I. Thermodynamical properties of Lennard-Jones molecules. *Physical review*, 159(1), (1967) p.98
- [43] R. W. Hockney, The potential calculation and some applications. *Methods Comput. Phys.*, 9, (1970) p.136.
- [44] P. Schofield, Computer simulation studies of the liquid state. *Computer physics communications*, 5(1), (1973), pp.17-23.
- [45] W. C. Swope, H. C. Andersen, P. H. Berens, and K. R. Wilson, A computer simulation method for the calculation of equilibrium constants for the formation of physical clusters of molecules: Application to small water clusters. *The Journal of Chemical Physics*, 76(1), (1982), pp.637-649.
- [46] S. Plimpton, Fast parallel algorithms for short-range molecular dynamics. *Journal of computational physics*, 117(1), (1995), pp.1-19.
- [47] H. C. Andersen, Molecular dynamics simulations at constant pressure and/or temperature. *The Journal of chemical physics*, 72(4), (1980), pp.2384-2393.
- [48] H. J. Berendsen, J. V. Postma, W. F. van Gunsteren, A. R. H. J. DiNola, and J. R. Haak, Molecular dynamics with coupling to an external bath. *The Journal of chemical physics*, 81(8), (1984), pp.3684-3690.
- [49] S. Nosé, A unified formulation of the constant temperature molecular dynamics methods. *The Journal of chemical physics*, 81(1), (1984), pp.511-519.
- [50] W. G. Hoover, Canonical dynamics: equilibrium phase-space distributions. *Physical review A*, 31(3), (1985), p.1695.
- [51] G. J. Martyna, D. J. Tobias, and M. L. Klein, Constant pressure molecular dynamics algorithms, *The Journal of Chemical Physics*, 101(5), (1994), pp.4177-4189.
- [52] H. C. Andersen, Molecular dynamics simulations at constant pressure and/or temperature. *The Journal of chemical physics*, 72(4), (1980), pp.2384-2393.
- [53] S. Le Roux, and V. Petkov, ISAACS—interactive structure analysis of amorphous and

crystalline systems. *Journal of Applied Crystallography*, 43(1), (2010), pp.181-185.

[54] A. R. Leach, *Molecular Modelling: Principles and Applications*. London: Addison–Wesley (1996)

[55] A. C. Van Duin, S. Dasgupta, F. Lorant, and W. A. Goddard, ReaxFF: a reactive force field for hydrocarbons. *The Journal of Physical Chemistry A*, 105(41), (2001), pp.9396-9409.

[56] S. Roy, J. Ryan, S. Webster, and D. Nepal. A Review of In-Situ Mechanical Characterization of Polymer Nanocomposites, *ASME Applied Mechanics Review* 69(5), 050802, Nov. 15, 2017, 18 pages.

[57] R. H. Rigby, M. H. Aliabadi, Mixed-mode J-integral method for analysis of 3D fracture problems using BEM. *Engineering Analysis with Boundary Elements*, 11(3), (1993) 239–256.

[58] W. Humphrey, A. Dalke, K. Schulten, VMD: visual molecular dynamics, *Journal of molecular graphics*, (1996); 14(1):33-8.

[59] F Liu, P. Ming, and J. Li. "Ab initio calculation of ideal strength and phonon instability of graphene under tension." *Physical Review B* 76, no. 6 (2007): 064120.